

The Polarization of Ambient Noise on Mars

E. Stutzmann¹ , M. Schimmel² , P. Lognonné¹ , A. Horleston³ , S. Ceylan⁴ , M. van Driel⁴ , S. Stahler⁴ , B. Banerdt⁵ , M. Calvet⁶, C. Charalambous⁷ , J. Clinton⁴ , M. Drilleau^{1,8} , L. Fayon⁹ , R. F. Garcia⁸ , D. Giardini⁴ , K. Hurst⁵ , A. Jacob¹ , T. Kawamura¹ , B. Kenda¹ , L. Margerin⁶, N. Murdoch⁸ , M. Panning⁵ , T. Pike⁷, J.-R. Scholz¹⁰ , and A. Spiga¹¹ 

Key Points:

- Seismic noise on Mars is polarized horizontally at low frequency (0.03–0.3 Hz) and vertically at high frequency (0.3–1 Hz)
- Polarization azimuth varies with local hour and season and follows the wind direction during the day
- Day polarization can partly be explained by pressure or acoustic emission and seismic wavefield may only be identified in the evening

Supporting Information:

- Supporting Information S1
- Figure S1
- Figure S2
- Figure S3
- Figure S4
- Figure S5
- Figure S6
- Figure S7

Correspondence to:

E. Stutzmann,
stutz@ipgp.fr

Citation:

Stutzmann, E., Schimmel, M., Lognonné, P., Horleston, A., Ceylan, S., van Driel, M., et al. (2021). The polarization of ambient noise on Mars. *Journal of Geophysical Research: Planets*, 126, e2020JE006545. <https://doi.org/10.1029/2020JE006545>

Received 4 JUN 2020
Accepted 24 NOV 2020

¹Institut de Physique du Globe de Paris, CNRS, Université de Paris, Paris, France, ²GEO3BCN-CSIC, Barcelona, Spain, ³School of Earth Sciences, University of Bristol, Bristol, UK, ⁴ETH, Zurich, Switzerland, ⁵Jet Propulsion Laboratory, California Institute of Technology, Pasadena, CA, USA, ⁶IRAP, CNRS, Toulouse, France, ⁷Department of Electrical and Electronic Engineering, Imperial College, London, UK, ⁸ISAE-SUPAERO, Toulouse University, Toulouse, France, ⁹Space Exploration Institute, Neuchâtel, Switzerland, ¹⁰Max Planck Institute, Göttingen, Germany, ¹¹Laboratoire de Météorologie Dynamique/Institut Pierre-Simon Laplace (LMD/IPSL), Centre National de la Recherche Scientifique (CNRS), École Polytechnique, École Normale Supérieure (ENS), Sorbonne Université, Paris, France

Abstract Seismic noise recorded at the surface of Mars has been monitored since February 2019, using the InSight seismometers. This noise can reach -200 dB. It is 500 times lower than on Earth at night and it increases of 30 dB during the day. We analyze its polarization as a function of time and frequency in the band 0.03–1 Hz. We use the degree of polarization to extract signals with stable polarization independent of their amplitude and type of polarization. We detect polarized signals at all frequencies and all times. Glitches correspond to linear polarized signals which are more abundant during the night. For signals with elliptical polarization, the ellipse is in the horizontal plane below 0.3 Hz. In the 0.3–1-Hz high frequency band (HF) and except in the evening, the ellipse is in the vertical plane and the major axis is tilted. While polarization azimuths are different in the two frequency bands, they both vary as a function of local hour and season. They are also correlated with wind direction, particularly during the daytime. We investigate possible aseismic and seismic origins of the polarized signals. Lander or tether noise can be discarded. Pressure fluctuations transported by wind may explain part of the HF polarization but not the tilt of the ellipse. This tilt can be obtained if the source is an acoustic emission coming from high altitude at critical angle. Finally, in the evening when the wind is low, the measured polarized signals may correspond to the seismic wavefield of the Mars background noise.

Plain Language Summary Seismic noise at the surface of Mars was unknown until the first measurements by the seismometers from the InSight mission in January 2019. On Earth, the microseismic noise (0.05–1 Hz) is composed dominantly of surface waves generated by the numerous sources related to ocean wave activities. On Mars, because there is no ocean, seismic noise is down to 500 times lower than on Earth reaching -200 dB in acceleration at night. In order to determine the nature of the Mars noise, we analyze its polarization with a statistical method and show that it is different to that on Earth. In the low frequency band 0.03–0.3 Hz, we detect signals with elliptical polarization in the horizontal plane. In the high frequency band 0.3–1-Hz (HF), signals have elliptical polarization in the vertical plane. The polarization ellipse azimuth gives the direction toward the source. On Mars, these azimuths are varying as a function of local hour and season and they are correlated with wind direction during the daytime. The HF polarized signals may be explained by local effects of pressure fluctuations and/or by acoustic emission coming from high altitudes in particular conditions. It is only in the evening when the wind is low, that the measured polarized signals may correspond to propagating seismic waves that would be the Mars seismic background noise.

1. Introduction

The InSight mission landed on the planet Mars on November 2019 (Banerdt et al., 2020; Lognonne et al., 2020) and deployed a seismic package (SEIS) which has recorded continuous seismic signals since February 2019. Seismic noise level is a crucial parameter for the success of the mission because marsquakes can only be detected when their amplitudes are above the station noise level (Giardini et al., 2020). Seismic

© 2020. The Authors.

This is an open access article under the terms of the Creative Commons Attribution License, which permits use, distribution and reproduction in any medium, provided the original work is properly cited.

noise is also of interest in itself to study the corresponding natural phenomena that excite the noise wavefield on Mars. It may correspond to propagating waves from sources yet to be discovered or it may be partly or completely controlled by local environmental effects. The origin of these local effects was extensively studied and modeled prior the mission launch and might be related to pressure ground deformation (Lognonné & Mosser, 1993), thermal effects (Van Hoolst et al., 2003), lander induced noise (Murdoch et al., 2017) as reviewed by Mimoun et al. (2017). If Mars seismic noise contains propagating waves, the noise might be useful for imaging the planet interior, from local scale (Berbellini et al., 2019; Romero & Schimmel, 2018), to global scale (Nishikawa et al., 2019; Schimmel, Stutzmann, & Gallart, 2011).

The seismic noise spectrum on Earth has a characteristic shape that can be observed everywhere on continents, on islands or at the ocean bottom (Stutzmann et al., 2009). The Earth noise spectrum has two peaks around 0.14 and 0.07 Hz called secondary and primary microseisms and a minimum between 0.05 and 0.005 Hz called hum. Sources of microseisms and hum are related to the ocean wave activity (e.g., Ardhuin et al., 2015; Hasselmann, 1963; Rhie & Romanowicz, 2006; Stutzmann et al., 2012; Tanimoto, 2007; Tanimoto et al., 1998). As there is no fluid ocean on Mars, similar microseisms and hum sources do not exist. Below 0.002 Hz, noise on Earth is caused by free air and inertial effects exerted by atmospheric perturbations on the sensor mass (Zürn & Wielandt, 2007). The density of Mars' atmosphere close to the surface is about 100 times less than on Earth, yet atmosphere-induced seismic signal, especially ground deformation induced by vortex-induced pressure drops have been reported by SEIS (Banerdt et al., 2020; Garcia et al., 2020; Kenda et al., 2020; Lognonne et al., 2020), as suggested by the prelaunch modeling and Earth tests (Kenda et al., 2017; Lorenz et al., 2015; Murdoch et al., 2017).

In 1976, a first seismometer recorded the seismic noise on Mars in the framework of the Viking mission (Anderson et al., 1977). The seismometer was located on the top of the lander and therefore it mostly recorded the response of the lander to the wind. To overcome this problem, which was also recorded before SEIS was deployed (Panning et al., 2020), the SEIS seismometers were placed on the ground and covered by a wind and thermal shield (WTS).

To determine the nature of the seismic noise recorded on Mars, one way is to analyze its polarization. On Earth, the polarization depends on the frequency band. Secondary microseisms are dominantly Rayleigh waves and their polarization is elliptical in the vertical plane (Haubrich & McCamy, 1969; Tanimoto & Rivera, 2005; Tanimoto et al., 2006). The ellipse back azimuth gives the direction toward the sources. Due to the continuously changing ocean wave activity, each seismic station simultaneously records Rayleigh waves from multiple sources. Therefore, statistical methods have been developed to analyze the secondary microseisms polarization and investigate the sources (Schimmel, Stutzmann, Ardhuin, & Gallart, 2011; Stutzmann et al., 2009). At lower frequency, Rayleigh and Love waves of primary microseisms and hum are equipartioned (Nishida, 2014; Nishida et al., 2008).

A first attempt to investigate the noise polarization on Mars was proposed by Suemoto et al. (2020) who analyzed data from sol 75 to 211. They showed a correlation with wind in agreement with Lognonne et al. (2020) and they identified P and Rayleigh waves in the frequency band 0.125–8 Hz. As shown below, we use a different method for measuring the polarization and we do not identify Rayleigh waves. In particular, the polarization that we measure below 0.3 Hz is in the horizontal plane which cannot correspond to Rayleigh waves. Clinton et al. (2020) analyzed the polarization of all detected events. They measured a polarization corresponding to P or S waves for some events and no Rayleigh waves could be identified.

To address the question of the nature of the seismic noise recorded on Mars, we monitor the continuous signal recorded by the three components of the broadband seismometer, SEIS, over the first year of the In-Sight mission. We analyzed the polarization in the frequency band 0.03–1 Hz. We do not investigate lander modes which are at higher frequency. We show that the polarization on Mars is very different than on Earth. We characterize the Mars noise polarization as a function of frequency and local time using a statistical approach. We then quantify the environmental local effect on the noise.

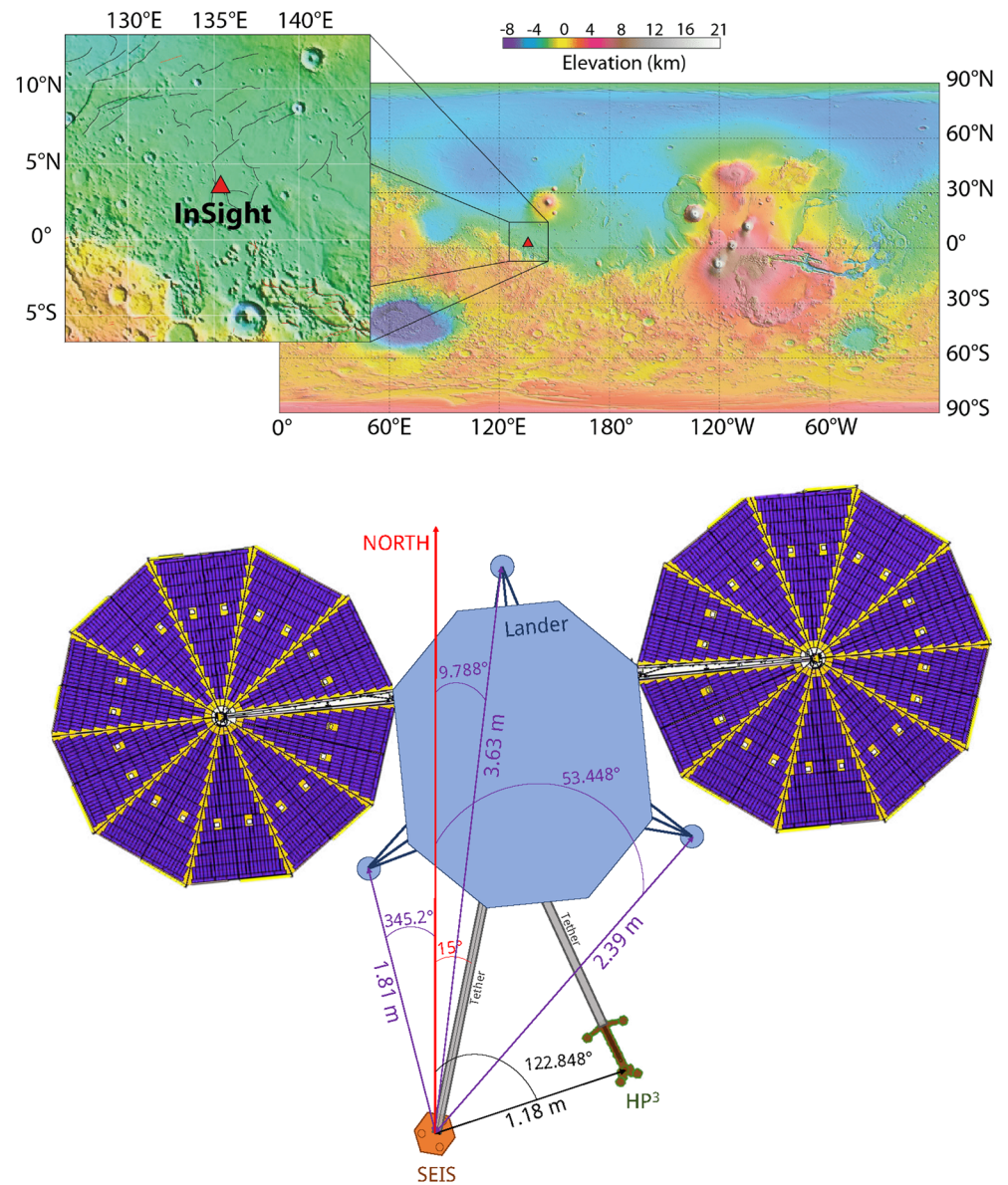


Figure 1. InSight lander and seismic station on Mars. The top plot shows InSight's location (red triangle) on the Mars topography map. The bottom plot is a sketch of the station and gives the position of the seismometer SEIS (orange) with respect to the lander (light blue) and its 3 feet (small circles), and with respect to the HP3 instrument (brown). The two solar panels attached to the lander are in dark blue and yellow.

2. InSight Mission Seismic Data

On November 26, 2018 InSight (Banerdt et al., 2020; Lognonne et al., 2019, 2020) landed on Mars. The lander is located in Elysium Planitia (Golombek et al., 2020), close to the equator (4.502°N, 135.623°E) in a flat area at an elevation of $-2,613.4$ m with respect to the Mars Orbiter Laser Altimeter geoid. The topography map (Figure 1, top) shows that the structure is flat around the station and toward the North and that the topography is higher with large craters toward the South. At the landing site, the topography is a gentle slope (less than 0.6°) down to the East (Golombek et al., 2020).

In January 2019, the three-component broadband and short period seismometers SEIS were placed on the ground, and a few weeks later they were covered by a WTS (wind and thermal shield). Figure 1 (bottom)

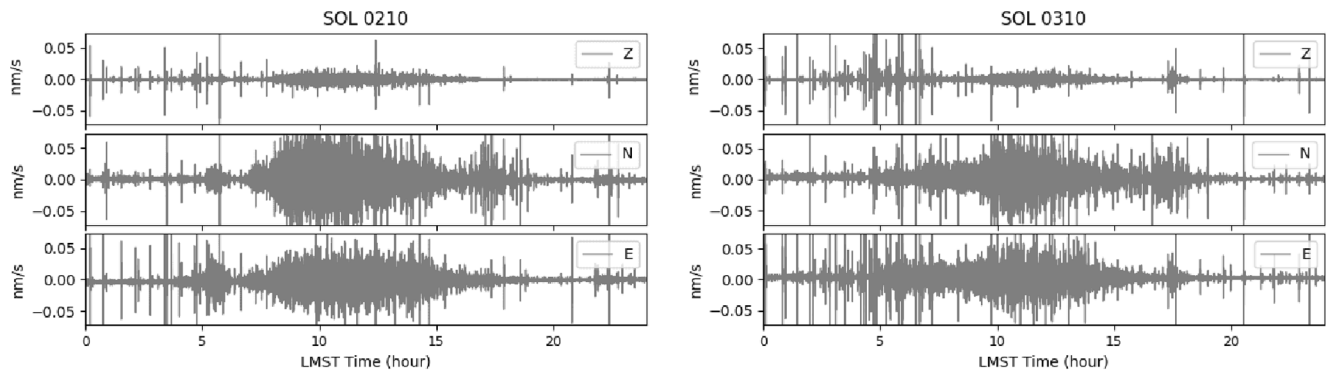


Figure 2. Continuous signals in velocity recorded by the three components of InSight's broadband seismometer on Mars (top: Z, middle: N, bottom: E). On sol 210 (left) and 310 (right) filtered between 0.03 and 1 Hz.

shows a sketch of the InSight station where we see that the lander is located to the North of SEIS. The distance between SEIS and the lander feet ranges from 1.81 to 3.63 m. The other instrument on the ground (HP³, the Heat Flow and Physical Properties Package) is to the East of SEIS. These azimuths and distances are important for the interpretation of the noise polarization.

Since mid-February 2019, the three components of the SEIS broadband seismometer have continuously recorded the ground motion. We present here the analysis of the continuous broadband seismic data (from Mars SEIS data service), from February 18, 2019 to April 13, 2020 which corresponds from sol 81 to 491. One sol is one day on Mars and corresponds to 24 h and 37 min UTC. Sol 0 is the day InSight landed on Mars. The three components U, V, W of the broadband seismometer are corrected from the instrumental response and rotated to obtain the Z, N, and E components. The North was determined by Savoie et al. (2020) and the corner frequency of the instrument is 0.1 Hz. Our analysis is restricted to frequencies below 1 Hz because above 1 Hz the continuous signals contain tick noise at 1 Hz and several lander modes (Ceylan et al., 2020) which are not investigated here. Data display similar characteristics every sol and Figure 2 shows the three components of the ground velocity recorded by the broadband seismometer for two sols, 210 (June 30 to July 1, 2019) and 310 (October 10–11, 2019) filtered between 0.03 and 1 Hz. We observe large amplitudes during the day and much weaker amplitudes at night on the three components. We also see numerous transient signals that are mostly glitches (Lognonne et al., 2020; Scholtz et al., 2020) or dust devils and wind gusts (Banerdt et al., 2020; Kenda et al., 2020; Lognonne et al., 2020).

Daily spectrograms are computed and Figures A1–A3 in the Appendix show spectrograms for sol 210 and 310 in which we observe similar diurnal variations for the two sols. Figure 3 (top plots) shows the probabilistic power spectral density (PPSD) in the frequency range 0.03–1 Hz, computed over sol 82–491. For comparison, the Earth high and low noise models are plotted with dashed line (Peterson, 1993) and the instrument self-noise (Lognonne et al., 2020) is shown in red. The PPSD and spectrograms are computed using ObsPy software (Beyreuther et al., 2010), following the classical method (e.g., McNamara & Buland, 2004) and data are cut in tapered windows of 1,000 s with 50% overlap. The vertical PPSD reaches a minimum of -200 dB in acceleration in the frequency range 0.1–0.5 Hz that is more than 50 dB (320 times) lower than the Earth LNM. This minimum is also close to the estimated instrument self-noise (red curve). The PPSD as a function of frequency has a V-shape that is very different to the noise PPSD on Earth. The PPSD slope is in $1/f^2$ at low frequency (LF) and f^2 at high frequency (HF), so the seismic spectrum amplitude varies like $1/f$ and f , respectively. The PPSD variability of 20–30 dB is related to the diurnal variations. Whereas the noise curve on Earth is known to be related to primary and secondary microseisms, the origin of the V-shaped noise curve on Mars is an open question. Comparing the three components, the minimum PPSD is at 0.15 Hz for the vertical component and shifted toward 0.3–0.4 Hz on the two horizontal components. Finally, Mars noise is below the Earth low noise model in the frequency range 0.1–0.6 Hz on all three components.

The median of the spectrograms as a function of local hour is shown in Figure 3 (bottom plots). For all three components, the minimum is reached in the evening (16:00–24:00) with values of -200 to -210 dB, and

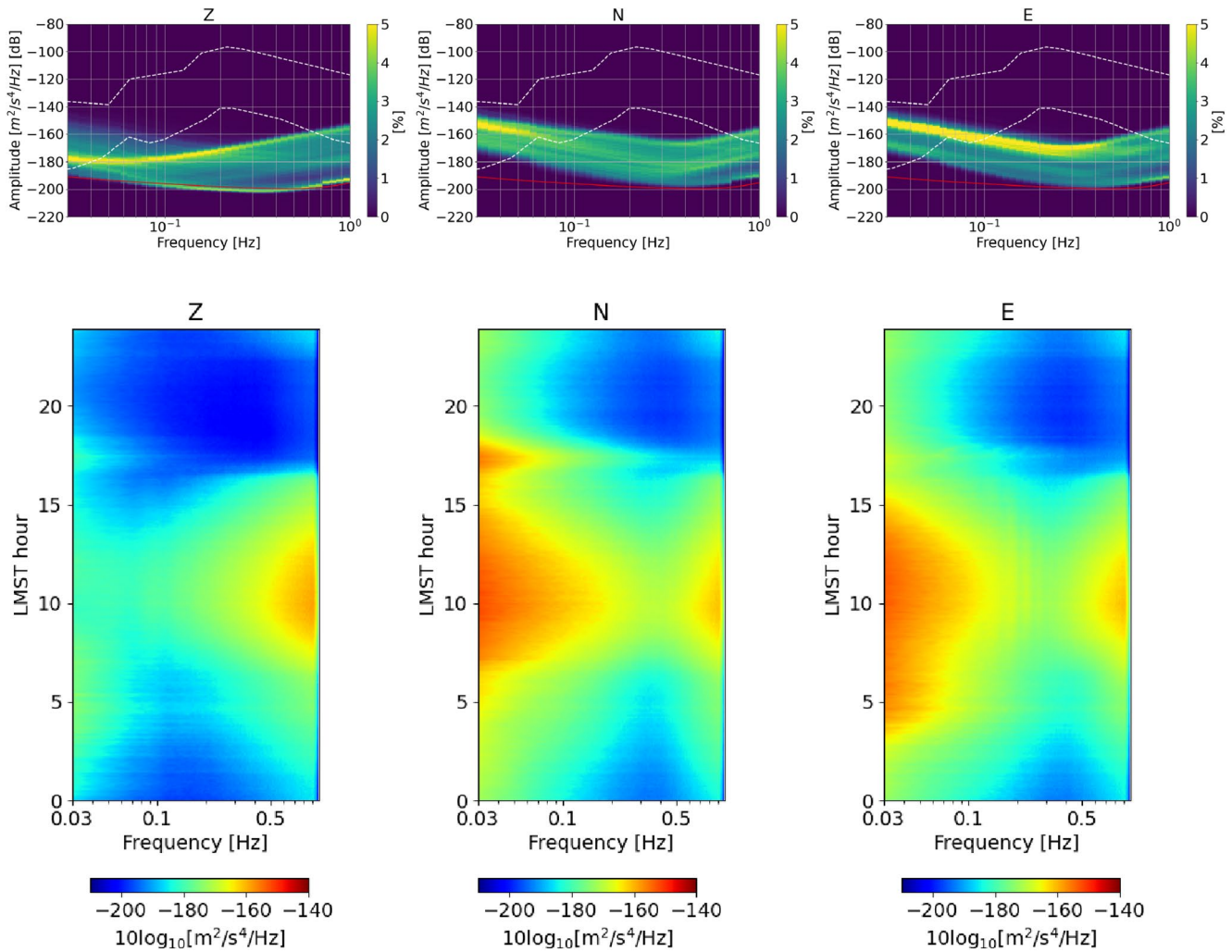


Figure 3. Average noise level recorded on Mars by the three components of InSight's broadband seismometer (left: Z, middle: N, and right: E) over sol 82 to 491. Top: Power spectral density in dB with respect to acceleration as a function of frequency. Earth low and high noise models from Peterson (1993) are shown with white dashed lines. The instrument self-noise is plotted in red line. Bottom: average spectrogram as a function of LMST local hour.

then in the morning (0:00-5:00) with -200 to -205 dB. The noise PSD is higher during the day (5:00-16:00) for all three components in the entire frequency band. Considering the pattern as a function of frequency, we see that above 0.3 Hz all three components have a similar amplitude and therefore polarization analysis is required to further investigate the particle motion. Below 0.3 Hz, the horizontal components have higher amplitudes than the vertical component and therefore the polarization will be mostly in the horizontal plane. Nevertheless, the similar noise amplitudes on the two horizontal components suggests that there is no systematic bias in either of the horizontal components and that they can be used to determine the azimuth of the ground motion.

3. Polarization Method

The polarization describes the three-dimensional particle ground motion at the station considering seismic records along the three directions (north-south, east-west, and vertical up-down). Schimmel, et al., (2011) proposed a method to analyze noise polarization as a function of time and frequency. As the noise on Earth consists dominantly of Rayleigh waves, they selected only signals with elliptical polarization in the vertical plane. For Mars, we extended this method to analyze linear and elliptical polarization in any direction.

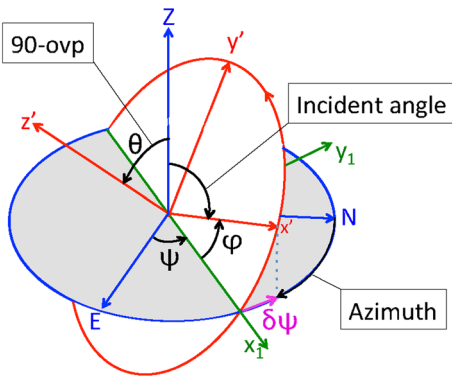


Figure 4. Sketch of the ellipse of polarization (red) with semi-major and semi-minor vectors \mathbf{x}' and \mathbf{y}' . The planarity vector \mathbf{z}' is perpendicular to the ellipse plane. The geographical axes are E, N, Z, and the Euler angles are ψ , φ , and θ . The ellipse of polarization is defined by three angles: (1) the semi-major vector azimuth with respect to North, (2) its incident angle with respect to the vertical, and (3) the “out of vertical plane” (ovp) angle. The ovp angle is 0° when the ellipse of polarization is in the vertical plane. The motion in the ellipse plane is from \mathbf{x}' toward \mathbf{y}' as indicated by the red arrow.

The three component signals are converted into time-frequency space using the S-transform (Stockwell et al., 1996) to build a time-frequency dependent cross-spectrum matrix. This matrix is then decomposed into three eigenvectors and eigenvalues for each time-frequency instance. These eigenvectors and eigenvalues are then used to find the instantaneous polarization attributes (e.g., Schimmel & Gallart, 2004) such as the semi-major and semi-minor vectors (\mathbf{x}' and \mathbf{y}') of the ellipse that best fit the ground motion (red ellipse in Figure 4). The planarity vector (\mathbf{z}') is defined as the cross product of the semi major and minor vectors and it is perpendicular to the plane of the ellipse. This vector contains also the information on the orientation of the particle motion which moves along the ellipse from the semi-major to the semi-minor along the shortest path. This motion can be pictured using the right-hand rule. If the right-hand thumb points into the direction of the planarity vector, then the fingers curl along the orientation of the motion. The polarization ellipse is described by three angles: (1) the incident angle of the semi-major vector, (2) the azimuth of the semi-major vector with respect to the North, and (3) the “out of vertical plane” (ovp) angle, which is the angle between the ellipse plane and the vertical plane. The ovp angle is 0° when the ellipse is in the vertical plane. Azimuths are measured from North toward East, from 0° to 180° , and there is an ambiguity of $\pm 180^\circ$ whenever the particle motion cannot be assumed to be retrograde or prograde.

In order to measure the stability of the polarization at each time-frequency, we compute the instantaneous degree of polarization (DOP) (Schimmel & Gallart, 2003, 2004). The DOP is an instantaneous quality measure based on the stability of an arbitrary polarization state with time. It is based on the fact that a high quality signal should not vary its polarization through the course of the signal or equivalently through a small sliding data window (Schimmel, Stutzmann, Arduin, & Gallart, 2011). We first compute the mean planarity vector over a given analysis data window (equivalent to a given duration of the signal). The DOP is then determined as the normalized sum of the scalar products between the instantaneous planarity vectors and the mean planarity vector. The DOP is equal to 1 for stable polarized signals and reaches 0 when the polarization is random. For linear polarization, the planarity vector is replaced by the semi-major vector for computing the DOP. This approach enables us to extract signals with stable polarization over time independent of their amplitudes. The detected signals can have large or small amplitudes. Weak signals with stable polarization will be extracted whereas more energetic signals with less stable polarization over time will be discarded. This approach is designed to extract polarized signals from a complicated wavefield, composed of a zoology of signals. Note that weak signals may not be detected with other methods based on a different definition for the DOP (e.g., Samson & Olson, 1980).

4. Polarization Analysis

We present the polarization attributes from when the seismometers were covered with the WTS, that is, after sol 81. We analyzed more than 1 year of data from sol 82 to 491, that is from February 18, 2019 to April 13, 2020. We start with the polarization analysis of data shown in Figure 2, for sol 210 and 310. Figure 5 (top) shows that the DOP is above 0.5 almost everywhere, which means that there are signals with stable polarization at most frequencies and during the entire sol. The polarization is more stable (DOP larger than 0.85) at low frequencies below 0.3 Hz, and mostly during the day (7:00 to 18:00). The exact start and end time of this diurnal stable polarization is slightly different between sol 210 and 310. We also observe high DOP values in the early morning (around 5:00) for both sols, and in the evening between 22:00 and midnight only for sol 210. For comparison, Figure A3 (Appendix) shows the DOP measured on Earth for the station SSB over 1 day. The DOP is lower on Earth (average DOP of 0.57) than on Mars (average DOP of 0.7) in the entire frequency band of interest, meaning that on average the polarization on Mars is more stable over several cycles than on Earth.

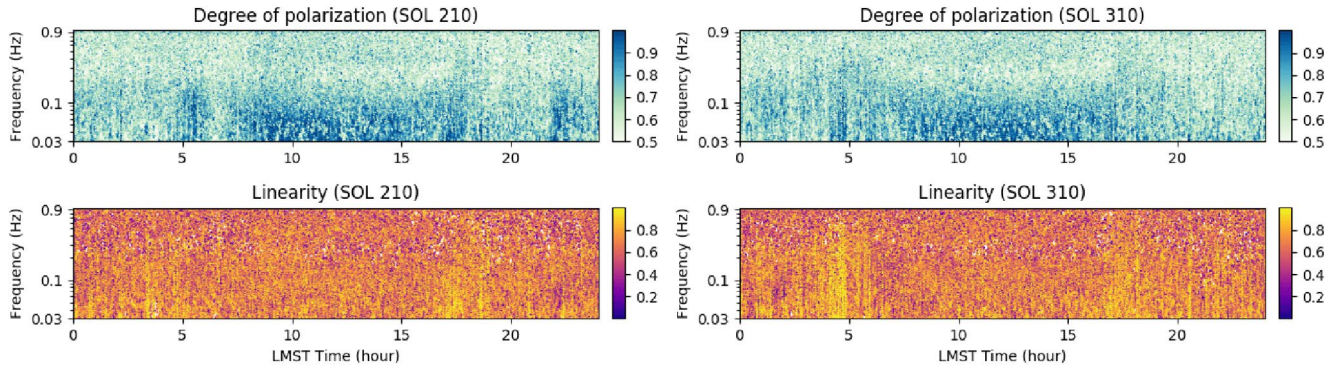


Figure 5. Degree of polarization, DOP, (top) and linearity (bottom) as a function of LMST time and frequency for sol 210 (left) and 310 (right). A higher DOP means that the signal polarization is more stable within the considered time-frequency window.

Figure 5 (bottom) shows the linearity of the polarization. We see that the polarization is mostly elliptical for frequencies above 0.3 Hz and slightly more linear at lower frequencies. We also see yellow vertical lines which correspond to signals linearly polarized in the entire frequency band for short duration. They mostly correspond to transient features and glitches that are clearly visible on the seismograms (Figure 2). For comparison, the polarization is more linear on Mars (average of 0.7) than on Earth (average of 0.5, Figure A3).

In order to better understand the noise polarization, we analyze separately linear and elliptical polarized signals. If the noise contains seismic waves, the corresponding polarization can be linear or elliptical. Body waves have mostly linear polarization whereas Rayleigh waves have elliptical polarization in the vertical plane. Nevertheless, in the case of interference of seismic waves from multiple directions, ground motion polarization becomes more complex.

We start with the linear polarization. We select signals with linearity higher than 0.97 and Figure 6 shows their incident angle and azimuth as a function of time and frequency for sol 210 and 310. Vertical lines visible on both the incident angle and the azimuth plots mostly correspond to the numerous glitches that can be identified on the seismic traces. The number of glitches varies from 1 day to another but they are more abundant at night. The azimuths are E-W in the morning and N-S at sunset. We remind the reader that azimuths are measured $\pm 180^\circ$. Glitch origin is still under debate (Lognonne et al., 2020; Scholtz et al., 2020). Apart from these signals visible in the entire frequency range, we also observe changes of polarization between day and night and between high and low frequencies. During the day and below 0.3 Hz, the detected signals are linearly polarized in the horizontal plane (incident angle close to 90°) with azimuth toward all directions. Those signals might correspond to atmospheric sources (Garcia et al., 2020; Kenda et al., 2020). At higher frequency (above 0.3 Hz), the incident angles are tilted with respect to the vertical axis, with an

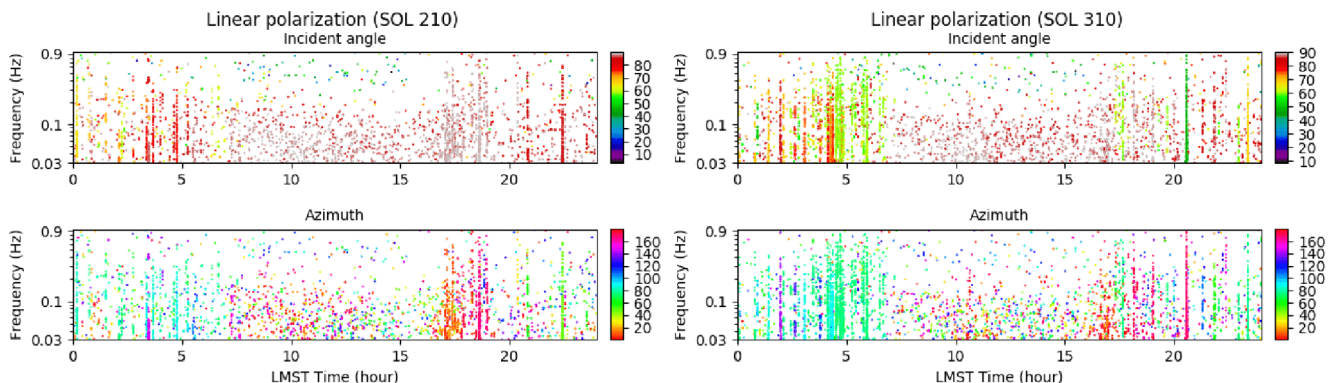


Figure 6. Incident angle and azimuth of signals with linear polarization as a function of LMST time and frequency for sol 210 (left) and 310 (right). The colors mark the incident and azimuth angles in degrees and are measured from the vertical and the North over East, respectively.

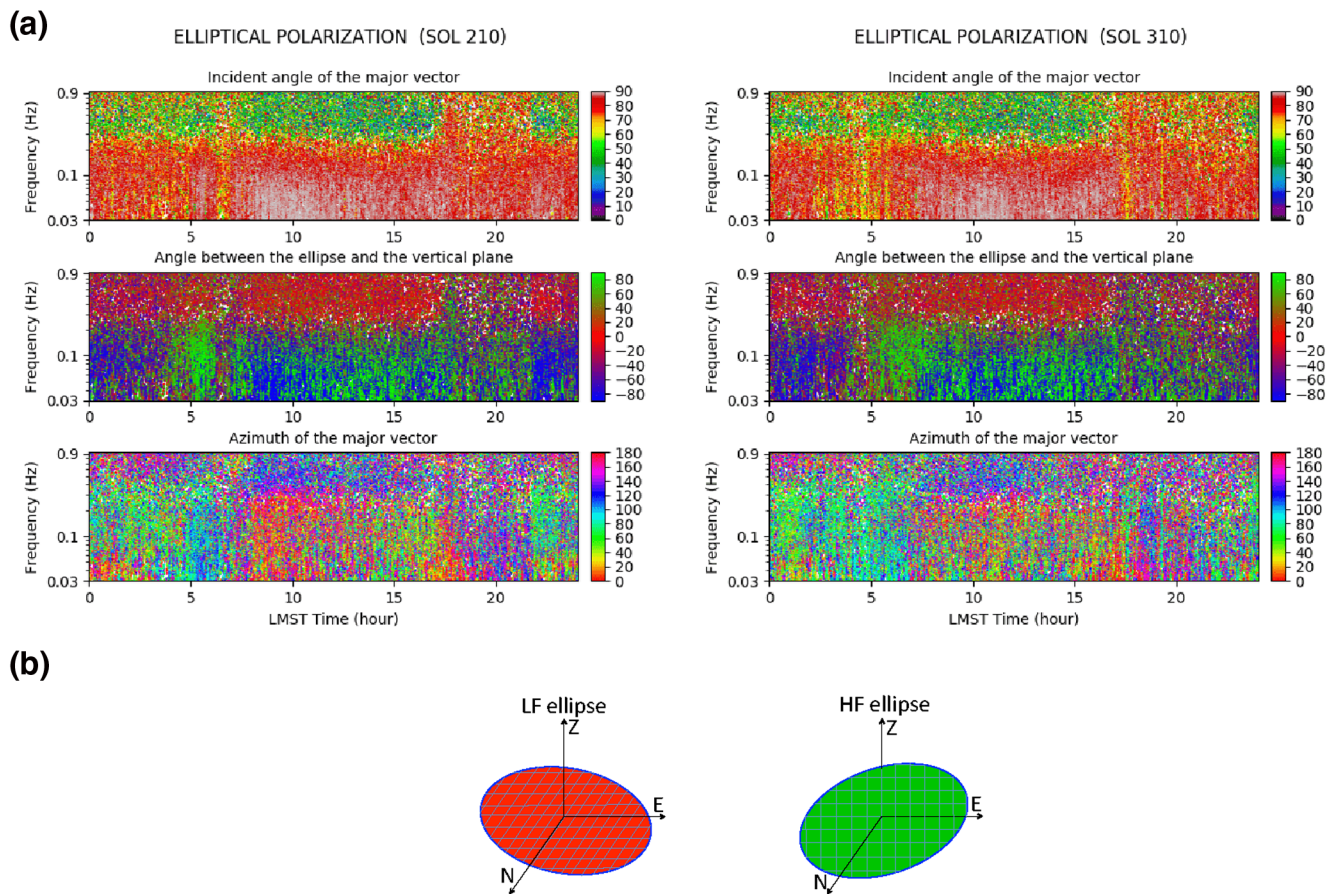


Figure 7. (a) For signals with elliptical polarization, incident angle of the major axis (top), angle between the ellipse and the vertical plane (middle), and azimuth of the major vector (bottom) as a function of LMST time and frequency for sol 210 (left) and 310 (right). Angles are all in degrees. Azimuth are between 0° and 180° with an ambiguity of 180° . A sketch of the high frequency horizontal and low frequency vertical ellipses of polarization is shown in (b).

angle of about 60° . At this stage, it is not possible to determine the origin of these linear signals but a lander origin is likely, as proposed prior to launch (Murdoch et al., 2017).

We now investigate signals with elliptical polarization and select signals with linearity lower than 0.9. The choice of 0.9 is arbitrary but any value around 0.8–0.9 does not change significantly the results. In order to determine the orientation of the polarization ellipse in the 3-D space, Figure 7a shows, for sols 210 and 310, the incident angle of the semi-major vector, the angle between the ellipse and the vertical plane and the azimuth of the major axis. The most striking feature in Figure 7 is the difference of elliptical polarization above and below 0.3 Hz.

Below 0.3 Hz, the major axis incident angle is close to 90° , that is horizontal (Figure 7a, top plots). The angle between the ellipse plane and the vertical plane (Figure 7a, middle plots) is close to $+90^\circ$ or -90° . This means that the particle motion is elliptical in the horizontal plane with clock-wise and anticlockwise motion during the entire sol. The only change in this frequency band is the azimuth which is rotating over the day (Figure 7a, bottom plots). On sol 210, the azimuths are toward N40E to N90E in the morning before 7:00, then they rotate to angles between 0 and N60E during the day (7:00 to 18:00). Around sunset, they are close to 120° , and at the end of the sol, they are again similar to morning azimuths. We observe similar azimuth variations on sol 310, but the time of azimuth changes are slightly shifted. On Earth, elliptical polarization in the horizontal plane is observed at lower frequency (below 0.04 Hz) and related to tilt (Koper & Hawley, 2010).

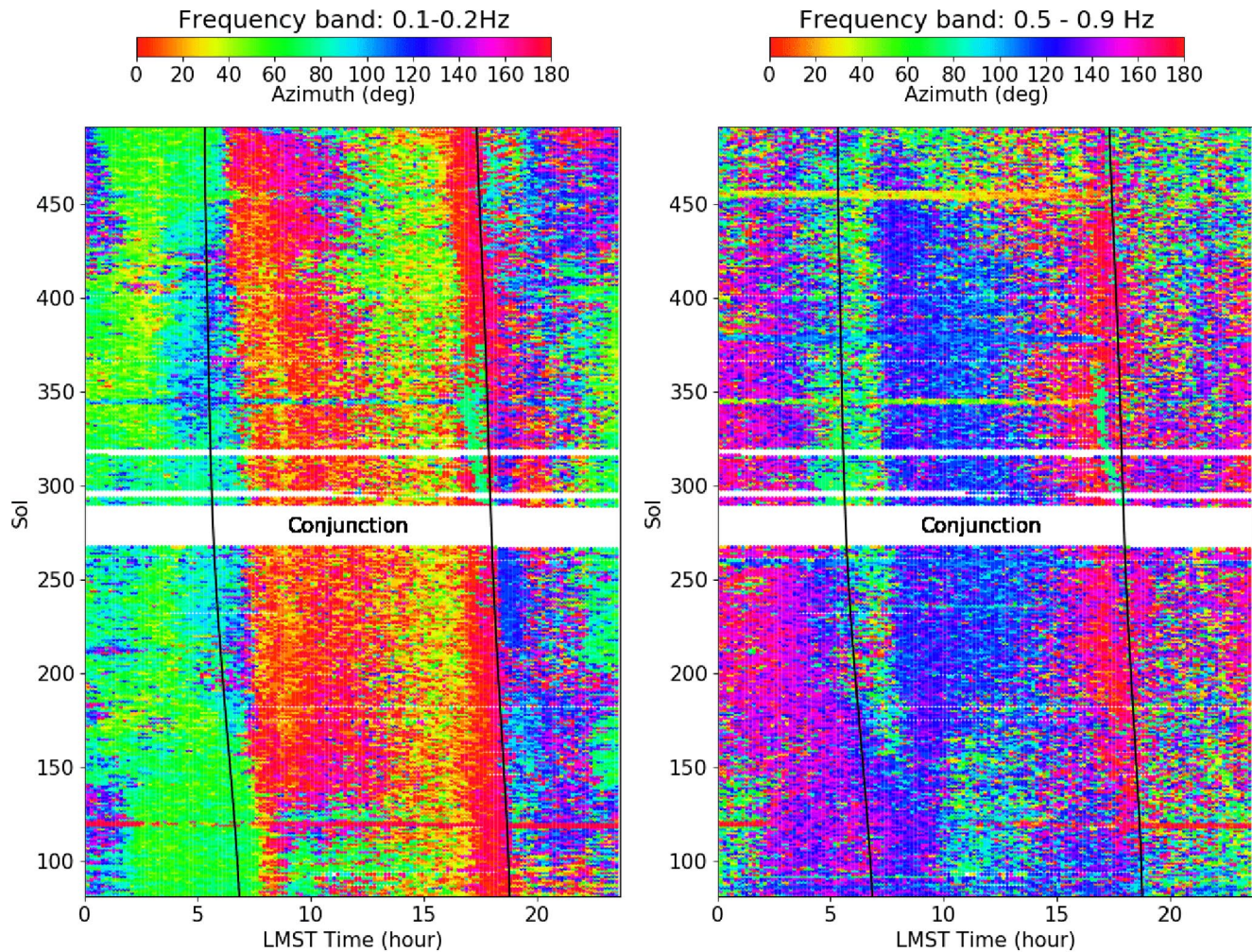


Figure 8. For signals with elliptical polarization, azimuth of the particle motion as a function of LMST time for sols 82 to 491. Frequency bands are 0.1–0.2 Hz (left) and 0.5–0.9 Hz (right). Summer solstice is on sol 308. Data were not available during conjunction. Black lines indicate sunrise and sunset times each sol.

Above 0.3 Hz, Figure 7a shows that the major axis incident angle is tilted with an angle of about 50° with respect to the vertical (top plots). The middle plot shows that the ellipse is in the vertical plane (angle of 0°). Finally, the ellipse azimuths are toward N120E–N140E during the day and no consistent azimuth can be determined at night. One striking feature is the change of polarization in the evening (18:00–21:00) which is more similar to what is observed at lower frequency. We note that it corresponds to the time when the signal amplitude is the lowest on the three components (Figure 3).

Figure 7b summarizes the elliptical polarization: above 0.3 Hz and except in the evening, the ellipse is in the vertical plane and the major axis is tilted with respect to the vertical axis; below 0.3 Hz, the ellipse is in the horizontal plane with clockwise and anticlockwise motion. These particle motions are far more complex than what we observe on Earth and, at this stage, propagating waves cannot be easily identified.

We similarly investigated all available data and observed that the discrepancy between HF and LF patterns is visible every sol. Figures S4–S7 in the Supplementary material show the frequency dependent particle motion azimuths from sol 82 to 491, which correspond to more than 1 year on Earth. To summarize these figures, we selected a HF band (0.7–0.9 Hz) and a LF band (0.1–0.2 Hz) and computed azimuth histograms as a function of time. Figure 8 shows the most abundant azimuths as a function of local time and sol. We retrieve the azimuth differences between day and night as in Figure 7, but we also see progressive changes of these azimuths as a function of increasing sols. Let us first consider the LF band. About 1 h after sunrise

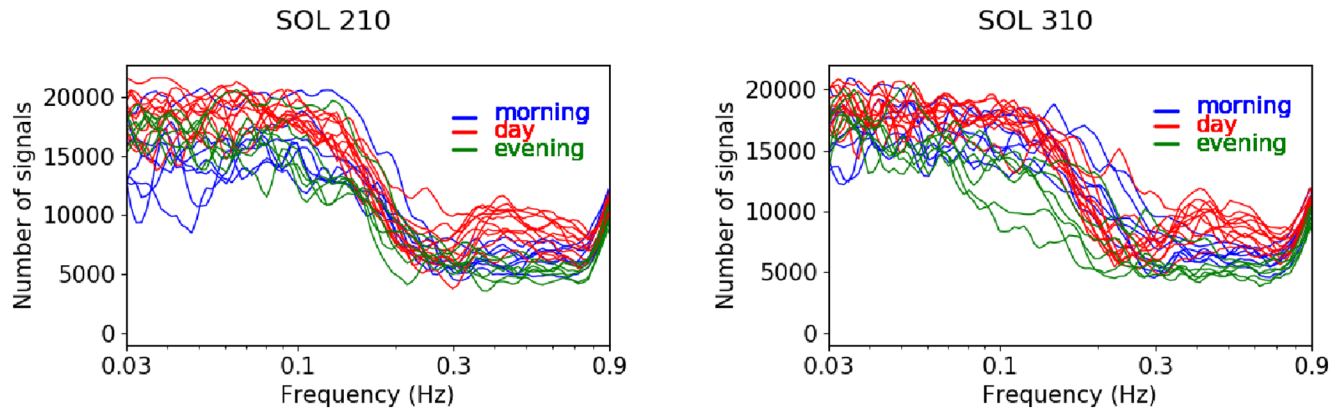


Figure 9. Number of polarized signals detected per hour as a function of frequency in the morning (0:00–7:00, blue curves), during the day (7:00–18:00, red curves), and the evening (18:00–24:00, green curves) on sol 210 (left) and 310 (right).

on the first sol (82), the azimuth changes abruptly from 60° to 0° . Later between sols 170 and 450, around sunrise the azimuths vary progressively from 60° to 110° before the same abrupt change. During the day, we also see progressive changes of the azimuths with increasing sols. One hour before sunset, the azimuth becomes dominantly N-S. At HF, azimuths are more scattered which can be confirmed by looking at the daily plots (Figures S4–S7). The azimuths are different from those at LF but they also progressively change with increasing sol. They are around 150° in the morning, progressively change to 60° around sunrise, then change abruptly to 120° 1 h after sunrise, and progressively change again to 0° just before sunset and remain very scattered from sunset to midnight. During part of the conjunction there were no data returned from InSight. Just after it, and up to sol 370, we observe for both HF and LF that, just before sunset, the polarization azimuths are around 60° . The azimuth similarity every sol and their progressive changes with increasing sols, may indicate that the detected signals are related to daily and seasonal changes. It may also indicate that these signals are not generated at the lander since it does not change its position. Indeed, the lander noise does not change in azimuth, but it changes in intensity related to the wind intensity and azimuth and to temperature. Lander eigenfrequencies also change over the sol but they are at higher frequency.

Finally, we investigated variations of the number of detected signals. Polarization attributes are computed for each time-frequency and a polarized signal is detected when the corresponding DOP is larger than 0.5. This threshold was determined on Earth but as the average DOP is larger on Mars than on Earth, we kept the same value. Figure 9 shows the number of polarized signal detected per hour as a function of frequency for sol 210 and 310. The absolute numbers depend on the definition of when a signal polarization is considered stable and are not important here as we compare only relative variations. We only considered signals with elliptical particle motion in order to exclude glitches. More polarized signals are detected at LF than at HF. After a minimum between 0.2 and 0.8 Hz, the number of detections increases again at higher frequency. We further see that at LF (below 0.3 Hz), we detect a similar amount of polarized signals at day and night. At HF (0.3–0.8 Hz), slightly more polarized signals are detected during the day and a bit less in the evening. We also observe some variability of the number of detections between sol 210 and 310. Finally, considering the entire frequency band, we do not detect significantly more signals during daytime.

5. Discussion

Our key observations are different elliptical polarization patterns above and below 0.3 Hz, azimuth changes over LMST hour that are different in the two frequency bands and slowly vary over sols, a similar amount of polarized signals during day and night at LF and slightly more during the day at HF. The polarization ellipse is in the horizontal plane below 0.3 Hz and tilted in the vertical plane above 0.3 Hz. Only in the evening, the polarization is the horizontal plane also above 0.3 Hz.

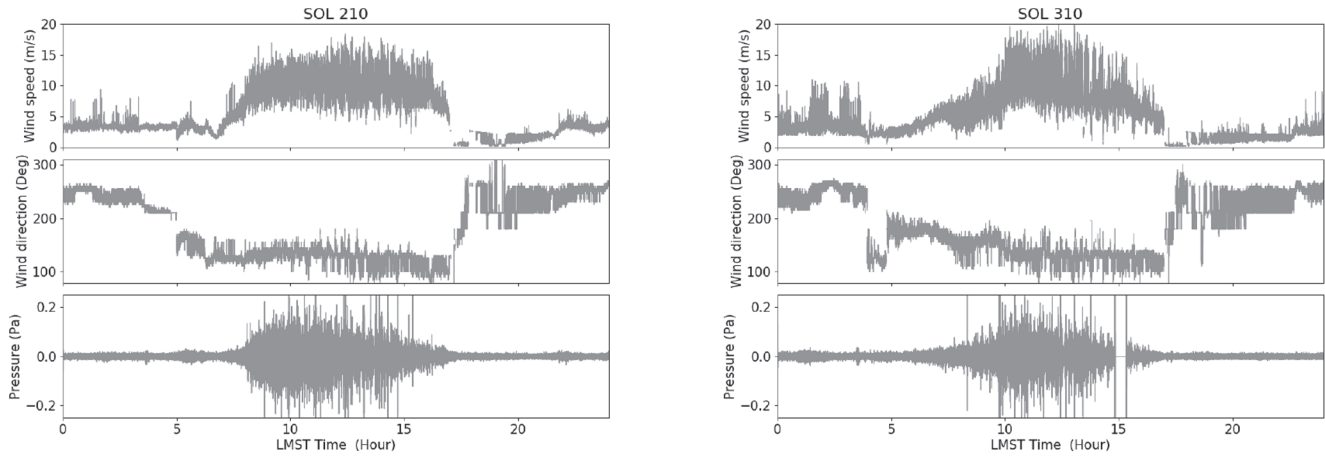


Figure 10. For sol 210 (left) and 310 (right), wind speed, wind direction, and pressure. Pressure is band-pass filtered between 0.03 and 0.99 Hz to be compared with seismic data. Sunrise is at 6:01 and 5:35 and sunset at 18:14 and 17:53, for sol 210 and 310, respectively.

On Mars, the seismic noise is likely generated by different phenomena related to local wind and pressure. Figure 10 shows for sol 210 and 310, the pressure filtered in the same frequency band as seismic data (0.03–1 Hz) together with the wind speed and wind azimuth as a function of local time. The pressure fluctuates a lot during daytime and much less at night (Banfield et al., 2020). We observe a steady increase of wind speed from after sunrise to sunset, high wind with high variability during daytime, and the wind almost stops in the evening (the “quiet zone” described in Banfield et al. (2020)). Figure 11 shows the relation between the wind speed and the three components of the seismic root mean square (rms) amplitudes as a function of LMST. Larger seismic amplitudes are observed for higher wind speeds. Furthermore the major vector azimuth of the polarization ellipse is relatively well correlated with the wind direction as will be shown further below.

Before investigating the possible origins of the measured polarized signals, we recall here the relationship between measured seismic amplitude and wind speed as proposed in the supplement of Giardini et al. (2020):

$$n^2 = (e^2 + (0.0058 \frac{\langle v^2 \rangle}{f^2} + 0.44 f^2 \langle v^2 \rangle)) 10^{-20} \text{ m}^2 / \text{s}^4 / \text{Hz}, \quad (1)$$

where n^2 is the seismic signal PSD, $\langle v^2 \rangle$ is the mean squared wind speed, e is the instrument self-noise (Lognonne et al., 2019), and f the frequency. Wind strength dependency is furthermore developed in Charalambous et al. (2020). The noise amplitude roughly follows a wind dependency at LF of $\sqrt{\langle v \rangle^2}$ and of $\langle v \rangle^2$ at HF. The frequency for which the two regimes equal depends on the wind speed and is about 0.3 Hz, 0.2 Hz, and 0.1 Hz for winds of 1.25, 3, and 10 m/s, respectively. We note that, the frequency of about 0.3 Hz is also the frequency that separates the two types of elliptical polarization either in the horizontal or the vertical plane in our polarization analysis.

In the following, we focus on the origin of the measured polarized signals, which can be aseismic or seismic. Aseismic phenomena can be as follows: (1) instrument self-noise, (2) sensor assembly (SA) and/or tether induced noise, (3) lander and wind shield noise, and (4) local pressure and wind effects. On the other hand, seismic polarized signals are due to propagating waves generated by natural sources. These sources may be in the atmosphere (5) or the solid planet (6). Let us now go through the different aseismic and seismic candidates for the observed signals in more details.

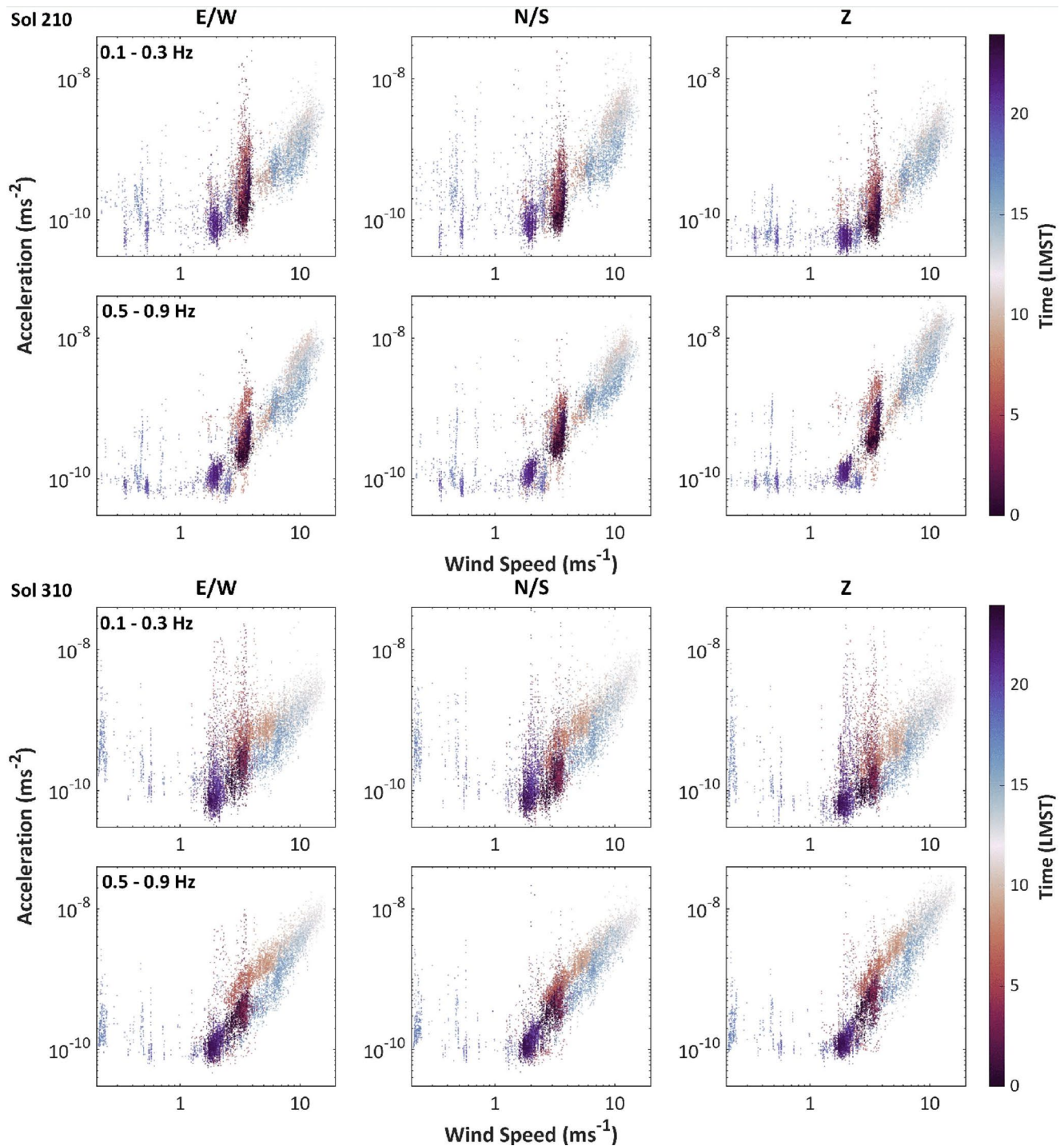


Figure 11. Seismic amplitude rms in acceleration as a function of local wind speed and LMST for each component E/W, N/S, and vertical in the frequency band 0.1–0.3 Hz and 0.5–0.9 Hz Sol 210 is shown on the top and sol 310 on the bottom. Colors correspond to the LMST hours.

5.1. Instrument Self Noise

In the evening and at HF, when the lowest noise PSD is reached (Figures 3, A1, and A2 in Appendix), the signal amplitude is close to the self-noise of the instrument (Lognonne et al., 2020). At frequencies larger than 0.01 Hz, the self-noise of each axis is however non-coherent in relation to the displacement

transducers and feedbacks of the VBB instruments (Lognonne et al., 2019), and cannot generate any stable elliptical polarization.

5.2. Sensor Assembly and Tether Induced Noise

The lander and the sensor assembly (SA) are connected through the tether and the load shunt assembly (LSA). The LSA serves as a buffer to disconnect lander and tether motions from the SA. The LVL is the leveling system of the SA capable of tilting the SA for centering and calibration purposes. The lowest and more damped mode frequencies of the LSA are about 5 and 8 Hz with low Q under Earth gravity and zero-slope condition (Lognonné et al., 2019). The mode frequencies of the LVL are much higher, 40 Hz or more and with larger Q of about 10 (Fayon et al., 2018). The modes of the LSA were measured on Mars during the last move of the pinning mass. The torsional mode of the LSA (9.5 Hz, $Q = 13$) and the longitudinal modes (2.86 Hz, 5.3 Hz, $Q = 25\text{--}35$) were again detected with different Q s. Future works will detail further the on-Mars calibrations.

A wind interaction with the tether or a wind interaction with the lander transmitted through the tether will generate a linear signal that is transmitted to the LSA and then to the SA. This signal will be attenuated as $\frac{\omega_{\text{LSA}}^2}{\omega_{\text{LVL}}^2}$ but will have a significant phase delay equal to the $1/Q$ difference between the LSA modes contributing mostly to the N, E, and Z directions.

The coherency of the seismic signals recorded on the vertical and horizontal directions could be associated to tilts or small rotation of the SA. These tilts or rotations are generated by the SA interaction with the environment, including reaction to forces generated by the tether and not damped by the LSA.

The three components of these coherent signals are however transmitted by LSA modes with different longitudinal, vertical, and transverse transfer functions. As soon as these modes have different Q , this can generate a phase delay between the two horizontal components and the vertical one. Although this will require complete and detailed modeling to confirm, the phase delay measured in radians is roughly equal to the difference of $1/Q$ between the LSA modes.

In the following, we test whether such configuration can explain the measured polarization for frequencies above 0.3 Hz, that is the inclined semi-major vector of the vertically polarized ellipses. In principle, the sum of an elliptical polarized signal with vertical or horizontal semi-major axis and a linear polarized signal with inclined motion can cause a signal with elliptical polarization and inclined semi-major axis. Therefore, we decomposed the measured elliptically polarized signals into the sum of an elliptical polarized component in the V-H plane and a linearly polarized component with small phase shift with respect to the elliptical ones. The decomposition process is described in Appendix.

This decomposition can be made for any phase delay between the elliptical and linear motion, the latter remaining not constrained by this decomposition. We took a phase delay of 0.15 radian corresponding to the phase shift between the torsional mode of the LSA ($Q = 13$) and the longitudinal or vertical modes ($Q = 25\text{--}35$) as measured during the pinning mass adjustment on Mars which excited the LSA modes (Hurst et al., manuscript in preparation). We restrict here the analysis to measured polarized signals with large linearity, between 0.85 and 0.95. It corresponds to small B/A ratio, (in the range of 0.05–0.15), where A and B are the length of the semi-major and semi-minor vectors of the polarization ellipse, as $B/A = 1 - L$. Results are shown in Figure 12.

The most interesting observation is a clustering of the azimuths of the elliptical component in the $30^\circ\text{--}40^\circ$ range and its perpendicular, between 120° and 130° with respect to the North (Figure 12, left). The first angle range is toward one foot of the SA. The H/V ratio of the elliptical components are mostly smaller than 1 above 0.5 Hz but tend to be larger than 1 below 0.5 Hz. All the signals have a linear component with larger energy than the elliptical one (Figure 12, middle). The azimuths of linear motion are more spread over all direction (Figure 12, right). These results support the phase delay between the longitudinal, vertical, and transverse reactions of SEIS's LSA as a candidate for part of the small ellipticity signals (in the range of 0.85–0.95 in linearity) in the frequency range 0.3–0.8 Hz. But very large phase shifts (e.g., signal with

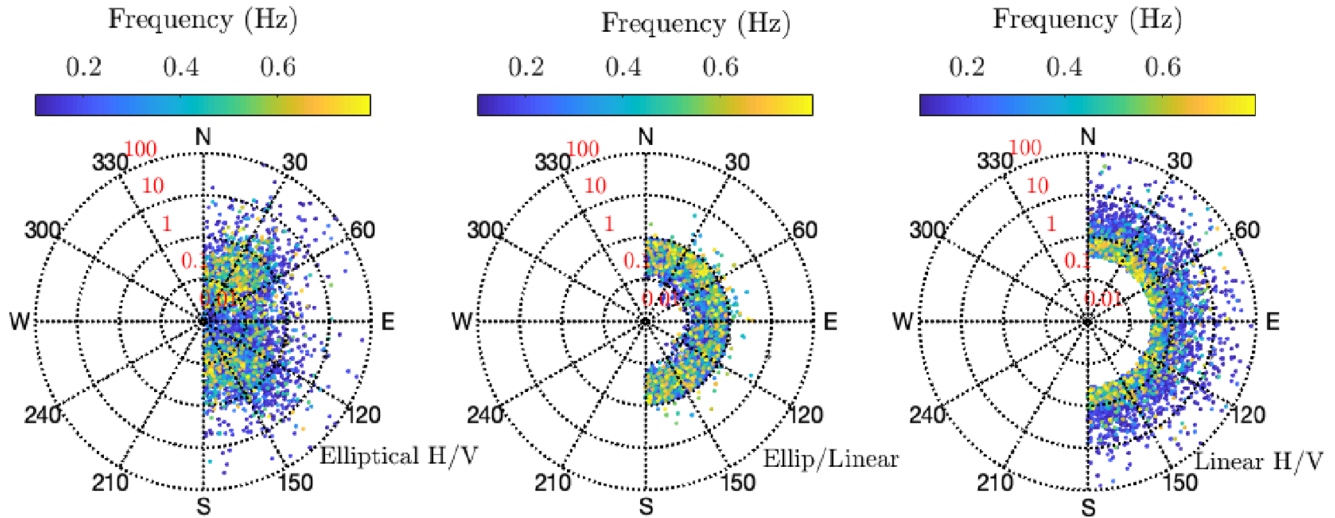


Figure 12. Decomposition of the elliptically polarized signals from sol 210 into elliptical and linear components assuming a phase delay of 0.15 radians between both components. From left to right are shown the H/V ratio of the elliptical components, the ratio between elliptical and linear component and the H/V ratio of the linear component. Shown are only polarized signals with degree of polarization larger than 0.75, frequencies between 0.3 and 0.8 Hz and linearity between 0.85 and 0.95 (B/A ratio between 0.05 and 0.15). This corresponds to signals with small but stable ellipticity. For the selected phase shift, a significant amount of elliptical components is found along the 30°–40° North azimuth and its perpendicular direction. Both, the elliptical and linear component have more signals with H/V ratio below one than above. Most of the signals have more energy on the linear component than on the elliptical component, tending toward equivalent energy at 0.8 Hz.

linearity smaller than 0.85) seem difficult to be explained by the LSA quality factors. A full amplitude model of the possible tether/LSA noise injection remains to be made.

5.3. Lander and Wind Shield Generated Noise

Both lander and wind-shield motions induced by wind are known to be sources of noise generating larger vertical than horizontal seismic amplitudes above ~0.3 Hz, as was suggested in prelaunch studies (Murdoch et al., 2017, 2018). The lander-generated noise is expected to be four times larger than the noise caused by the wind shield. The excitation source is mostly wind drag on the lander and wind shield and therefore depends on the wind square velocity (v^2 , Equation 1) for the HF noise. In addition to that, the lander also generates resonances observed above 1 Hz (Giardini et al., 2020; Lognonne et al., 2020), which are above the frequency range of this study.

The drag noise is generated through static loading on the ground of both the three lander feet and the wind shield. The drag of the wind shield generates displacement of the three axes of the SEIS seismometer. The prelaunch estimation of this noise predicts, however, small noise amplitudes. For the vertical noise PSD, n_z^2 , the proposed dependency is:

$$n_z^2 = \left(0.024 \left(\frac{v_{s0}}{v_s} \right)^2 \langle v^2 \rangle^2 f^{2/3} \right) 10^{-20} \text{ m}^2 / \text{s}^4 / \text{Hz}, \quad (2)$$

where we set the square wind-velocity rms $\langle v^2 \rangle$ during 95% of the day to $7.2^2 \text{ m}^2/\text{s}^2$, as obtained from the integration of the wind-squared amplitude spectrum between 0.1 mHz and 1 Hz. v_s is the ground shear velocity, while $v_{s0} = 150 \text{ m/s}$ is the reference velocity used by Murdoch et al. (2017) and f is the frequency in Hz. Using ground shear velocities of about 70 m/s, the model provides both smaller vertical noise than observed (by a factor of 2 in amplitude), as well as a different frequency dependency in the HF regime, although the latter being related to hypothesis in the wind turbulence spectrum, to be refined with new data.

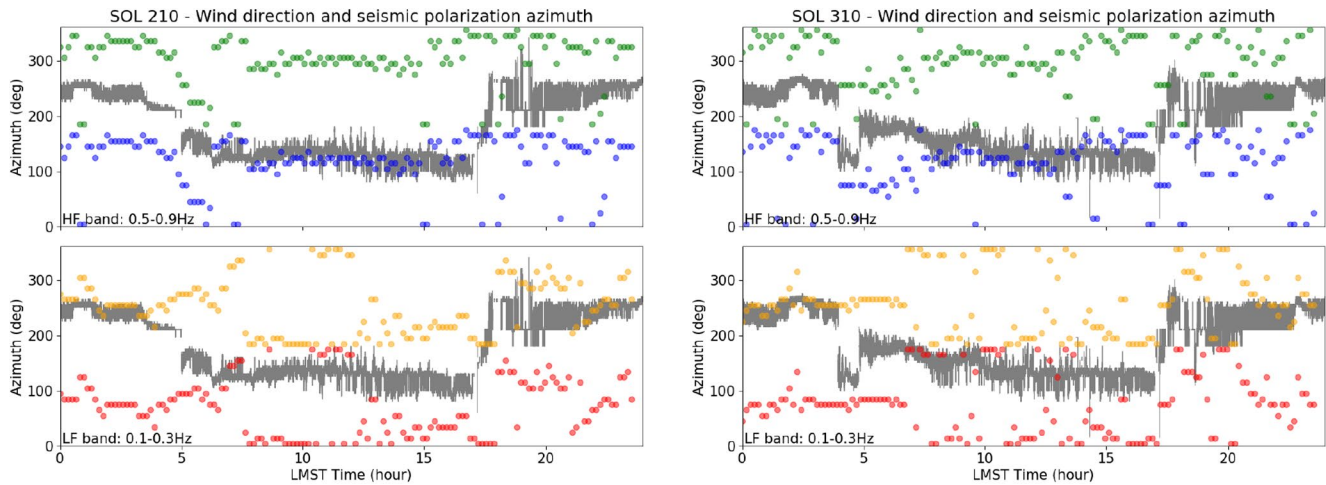


Figure 13. Polarization azimuths (color) in the frequency band 0.5–0.9 Hz (top) and 0.1–0.3 Hz (bottom) and wind azimuth (gray) for sol 210 (left) and 310 (right). Measured azimuths are plotted in blue and red and these angles $+180^\circ$ are in orange and green, respectively.

This model, however, generates no phase shifts between the E, N, Z noise components and therefore cannot cause elliptically polarized motions. Phase shifts might however be generated due to the distance between the two solar panels and the lander body. This may happen if their excitation is generated by traveling wind/pressure perturbations reaching the two solar panels at different times (i.e., with phase delay) (Murdoch et al., manuscript in preparation). The largest lander effects may then occur in the low wind night conditions, when the wind blows in the direction of the azimuth of the solar panels and at short periods where the phase shift would be maximum. In that case it is expected that the ellipticity of the polarized signals increases with frequency. This is not what we observe for three reasons. First, the HF linearity is not decreasing at night (Figure 5). Second, the wind directions during night are varying with season (Banfield et al., 2020; Spiga et al., 2018). And third, we showed that the number of polarized signals between morning, evening and day is relatively comparable, even if the wind speed and azimuth are significantly changing.

In conclusion, we do not consider the lander generated noise as the primary source of elliptically polarized noise, even if a full model needs to be developed to confirm this hypothesis. Lander and WTS can nevertheless contribute significantly to the linear noise, especially those with a clear wind-square amplitude dependency, as demonstrated by Charalambous et al. (2020).

5.4. Pressure Fluctuation Transported by the Environmental Wind

We focus here on the effect of local pressure fluctuations carried by the environmental wind. During the daytime, the local pressure variations generate a compliance effect on the vertical component and tilt mostly visible on the horizontal components (Banerdt et al., 2020; Lognonne et al., 2020). Such an effect is observed on Earth at longer periods (e.g., Roult & Crawford, 2000) and also at the ocean bottom (e.g., Crawford et al., 1991). On Mars, compliance and tilt are best observed when dust-devils (convective vortices) pass close to the InSight station (Banerdt et al., 2020; Kenda et al., 2020). On sol 210, 34 convective vortices were detected during the day-time.

Pressure fluctuations carried by the environmental wind can generate elliptically polarized signals in the vertical plane that are distinct from the linear ground deformation due to the pressure static loading (e.g., Farrell, 1972). The noise carried by wind has been proposed as one of the major sources of VBB recorded noise below 1 Hz (Garcia et al., 2020; Kenda et al., 2020; Lognonné & Mosser, 1993; Lognonne et al., 2020). This is furthermore supported by the strong correlation of the azimuth of the polarized signals with wind direction which is particularly striking during daytime in both high and LF bands (Figure 13). It has also been illustrated in Lognonne et al. (2020) and Charalambous et al. (2020).

Sorell's theory (Sorrells, 1971) was developed for Mars by Kenda et al. (2017). Kenda et al. (2020) showed clear correlation between seismic signal and pressure in the frequency range 0.03–0.8 Hz and used it for

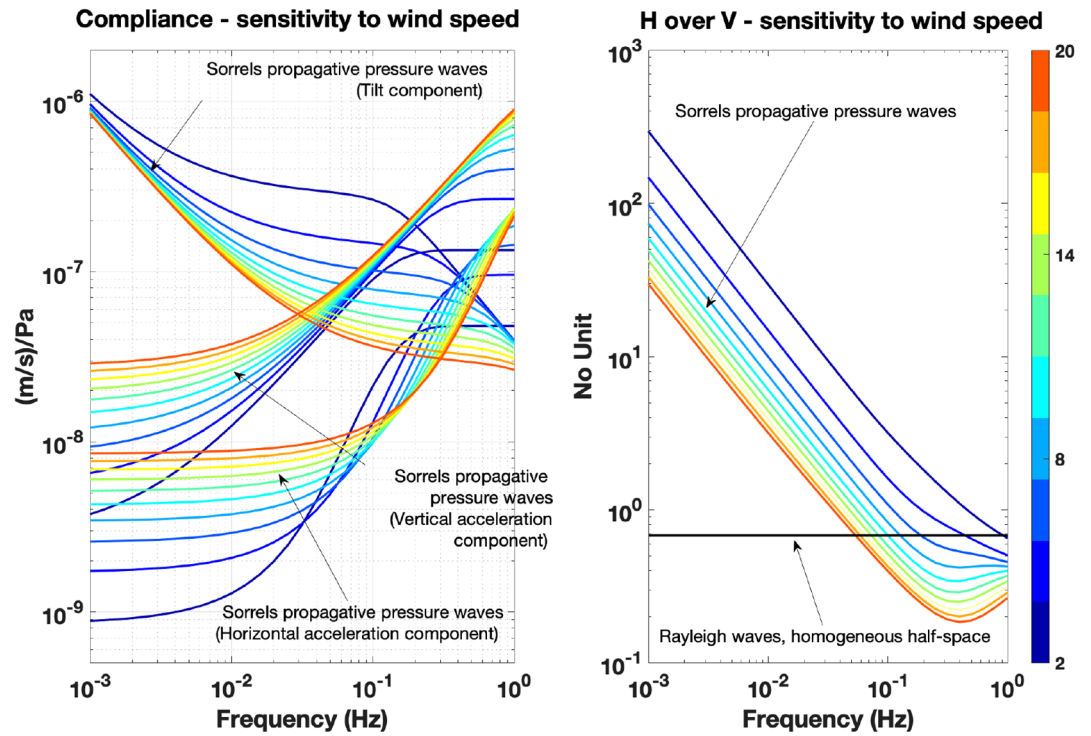


Figure 14. Vertical and horizontal compliances for the two layer model of Kenda et al. (2020). The first layer is 5 m thick with V_p and V_s of 198 and 118 m/s, while the second layer is a semi-infinite layer with V_p and V_s of 926 and 512 m/s, respectively. This model averages the more complex model proposed by Lognonne et al. (2020). The horizontal acceleration is the sum of both the horizontal tilt and of the horizontal ground acceleration and converted to ground velocity. Together with the vertical ground velocity, they are shown for different wind velocities as a function of frequency on the left figure. The color bar represents the range of wind values from 2 to 20 m/s. The right figure shows the amplitude of the H/V ratio. The phase of the H/V for a layered model is the same as for a homogeneous model and equal to $-i$.

estimating the subsurface structure below the lander (Kenda et al., 2020). Following Sorrells (1971), pressure waves propagating at wind speed c will generate elliptically polarized signal in the vertical plane. If the pressure wave is propagating horizontally, it can be expressed as $p(x, t) = p_0 e^{i\omega(t-x/c)}$. Then, for a homogeneous half-plane, the resulting seismic signal H/Z ratio is given by:

$$\frac{H}{Z} = \frac{v_s^2 + v_p^2 \frac{g}{c\omega}}{iv_p^2}, \quad (3)$$

where H and Z are the horizontal and vertical seismic displacements, v_p , v_s are the ground P and S velocities, g the Martian gravity, and ω the angular frequency, respectively. The term $1/i$ corresponds to a $\pi/2$ phase shift between horizontal and vertical components and therefore the polarization is elliptical in the vertical plane.

Considering a depth dependent structure of Mars, the compliance H/V ratio becomes frequency dependent and is affected to first order by larger seismic velocities due to compaction in the first 10 m. This is illustrated in Figure 14 with the simple two-layer model developed by Kenda et al. (2020). The H/Z ratio is minimum for winds larger than 4–5 m/s close to frequency of 0.5 Hz, with H/Z amplitude ratio in the range of 0.2–0.5. This ratio is larger than one at lower frequency for almost all wind regimes. The ellipticity of the signal is therefore expected to vary with frequency and wind speed.

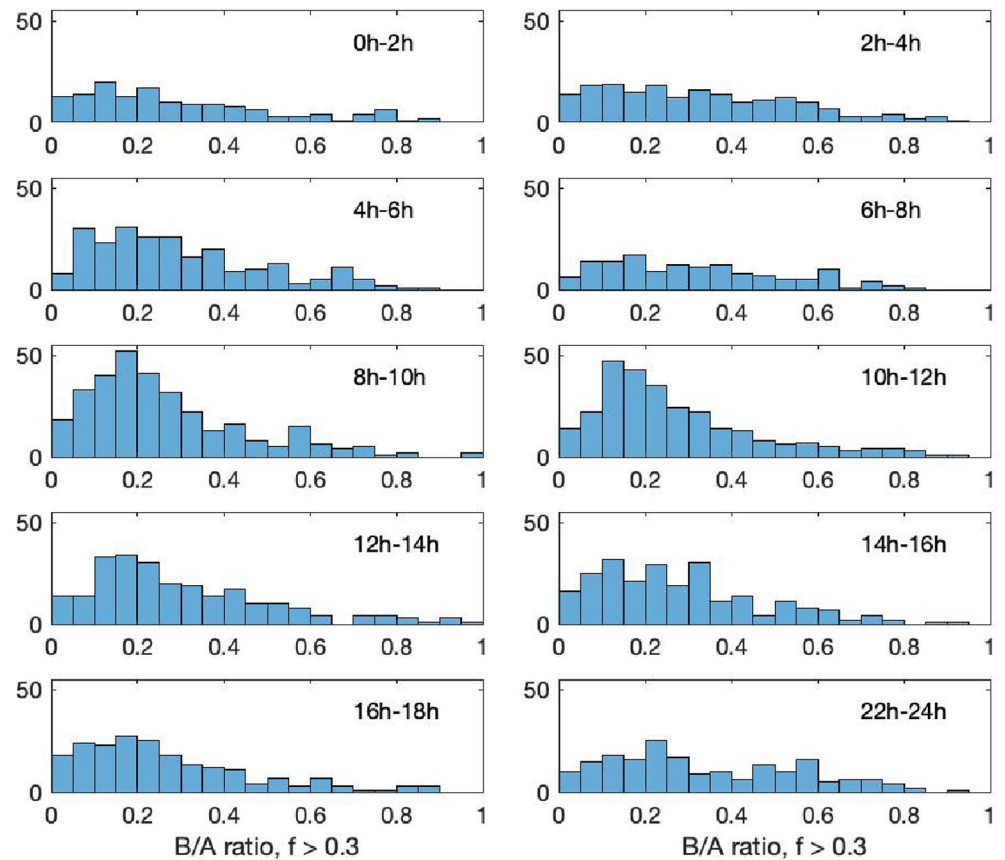


Figure 15. Histograms of the B/A ratio of the detected signals for sol 210 and frequencies above 0.3 Hz, when the polarization ellipse is in the vertical plane, that is from LMST hour 0–18 and 22–24. Only signals with degree of polarization larger than 0.8 are shown. For the large wind regime, between LMST hours 8 and 14, histograms have a clear peak for B/A of about 0.2.

At some frequencies and wind velocities, the compliance H/Z ratio can be comparable in polarization to a Rayleigh wave. Indeed, a Rayleigh wave has a H/Z ratio of about $\frac{2}{3i}$ in an homogeneous medium and this ratio becomes frequency dependent when layered structure is considered. For Rayleigh waves and for compliance, polarization is always in the vertical plane and the two ellipse axis are vertical and horizontal. Differences between compliance polarization to Rayleigh wave polarization are that compliance polarization (1) is phase velocity dependent, (2) is correlated with pressure, (3) has a H/Z ratio that varies with wind speed, and (4) has a different H/Z amplitude ratio than Rayleigh wave polarization.

Let us now consider the dependency of the measured linearity (L) as a function of wind speed. If it varies with wind speed, the polarization cannot correspond to Rayleigh waves. We focus on sol 210 and we consider only the frequency band above 0.3 Hz, that is when the polarization ellipse is in the vertical plane. We exclude the LMST time between 18:00 and 22:00 LMST time because the polarization is in the horizontal plane. We select DOP larger than 0.8 to keep the very stable polarization. Figure 15 represent the histograms of the B/A ratio of the ellipse values as a function of local time, where A and B are the length of the semi-major and semi-minor vectors. B/A ratio corresponds to $1 - L$. When the wind is large, between 8 and 14 h local time, a peak with a B/A ratio of 0.2 is found, while for lower wind, the dispersion of the B/A ratio is wider. Although the B/A in windy period is comparable to the expected H/Z ratio shown in Figure 14, the incidence of the semi-major axis is tilted with respect to the vertical axis (see Figure 7) in a way not predicted by the 1-D pressure loading theory of Sorrells (1971).

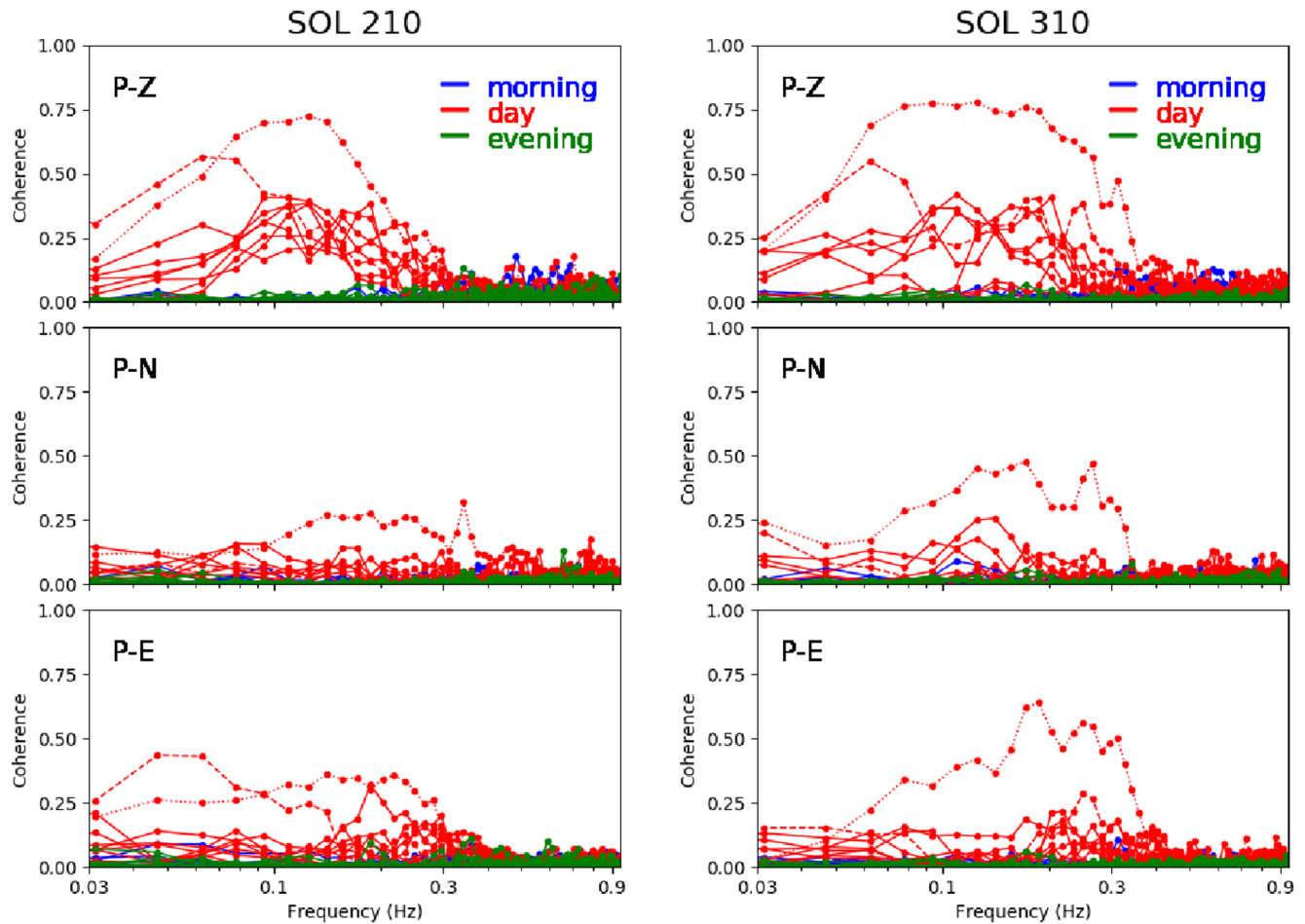


Figure 16. Coherence between pressure and seismic velocity as a function of frequency for each component: vertical (top), N-S (middle), and E-W (bottom) for sol 201 (left) and sol 310 (right), considering windows of 1 h each. Dashed and dotted lines correspond to LMST hours 12 and 14 for sol 210, 13, and 9 for sol 310 for which coherence is the highest.

A potentially misleading observation is the lack of coherence between VBB signals and pressure signal apart from the active daytime activity, as already noted in Lognonne et al. (2020), Garcia et al. (2020), and Kenda et al. (2020). Figure 16 shows the coherence between each seismic component and pressure in 1 h windows. It illustrates that the coherence with pressure is much less during the evening and night time and at high frequencies. Coherence with pressure is low for all three components of frequencies above 0.3 Hz day and night. The coherence is also low below 0.3 Hz at night when the pressure variability is low. During the day, the coherence with pressure increases between 0.04 and 0.2 Hz, and the largest effect is observed on the vertical component.

The lack of coherence must however be taken with care in any argument rejecting pressure waves during the evening or night. This is illustrated by Figure 17 which shows, based on the VBB mean noise shown by Lognonne et al. (2020), the amplitude of the pressure fluctuations necessary to generate these noise levels. Only those during the day time are well above the minimum noise level of the pressure sensor reported by Banfield et al. (2020). That minimum noise level can be either the pressure sensor self-noise or other source of pressure fluctuation not generating seismic polarized ground deformation. In all cases, and if we assume that Sorrells noise is a potential source above 0.2 Hz, this will explain the lack of coherence during the evening and night between the VBB signal and the pressure signal.

Sorrells' theory predicts seismic noise polarization that is frequency-dependent. This frequency dependence comes from the compliance model, from the propagating pressure fluctuation and from the variation of the

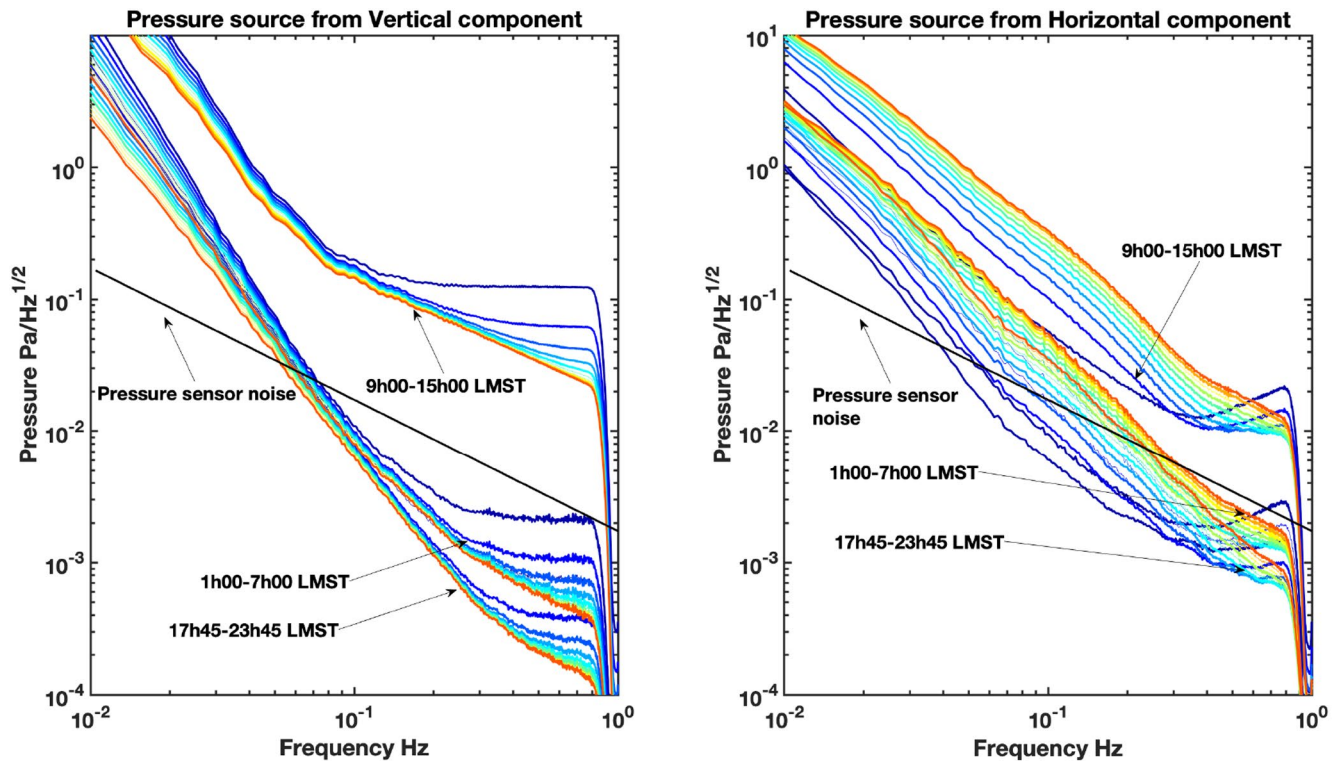


Figure 17. Estimation of the pressure noise able to generate typical SEIS noise levels for different wind conditions. The three typical SEIS noise levels, from lowest to highest in acceleration spectral amplitude, are those of the late evening (17:45–23:45 LMST), night (1:00–7:00 LMST), and day (9:00–15:00), as provided by the supplement 1 of Lognonne et al. (2020). This is shown on the left for the vertical VBB component and on the right for the VBB horizontal component. The black line shows the lowest pressure noise spectra recorded by the InSight pressure sensor (Banfield et al., 2020). This shows that the SEIS noise, if due to pressure wave and above 0.1 Hz, needs, for the vertical axis, pressure much less than the resolution of the pressure sensor under evening and night conditions. The necessary pressure on the horizontal components are however detectable for frequencies smaller than 0.2 Hz in the night. They are also always above the pressure sensor noise level during day conditions, which allows some pressure decorrelation during this period (Garcia et al., 2020).

environmental wind. In a 1-D homogeneous half space, the compliance is not frequency-dependent. Considering a layered model with increasing rigidity with depth, the vertical component compliance roughly increases like $f^{0.7}$ until a corner frequency in the range of 0.5–1 Hz depending on the wind (Figure 14, left). For the pressure, observations suggest a slope of about -1.7 (Banfield et al., 2020) in power and -0.85 in amplitude spectrum.

The two effects of compliance and pressure amplitude spectrum compensate and lead, for a stable wind, to a roughly flat spectrum in vertical ground velocity until the compliance corner frequency and therefore a f -spectrum in vertical seismic acceleration. Nevertheless, this corner frequency is strongly dependent on the first meters of the ground structure and could easily be moved above 1 Hz even for low wind velocity. Therefore, we do not discuss the comparison with observed seismic spectrum above 0.3 Hz. At LF ($f \leq 0.1$ Hz), Sorell's theory predicts an elliptical motion in the vertical plane and now the semi-major axis is horizontal (Figure 14, right). This is not the LF observed polarization which is in the horizontal plane. Also, the pressure only cannot explain the observed $1/f$ vertical component seismic spectrum amplitude ($1/f^2$ in PSD, Figure 3) at LF and the stability of the wind needs to be considered for generating observations and/or injection of horizontal noise on the vertical, as the latter have amplitude variations like f^{-1} at long period due to tilt effects.

In conclusion, whereas pressure waves are a good candidate for explaining the amplitude of the seismic signals and have been well-modeled for large pressure drops (Banerdt et al., 2020; Kenda et al., 2020; Lognonne et al., 2020), they cannot explain the observed polarization, neither the horizontal polarization at LF, nor the inclined polarization in the vertical plane at HF. Possibly, local lateral heterogeneities, as for

instance the Homestead hollow (Golombek et al., 2020), may explain this polarization but this has not been investigated here.

5.5. Acoustic Emission

In the previous section, we considered the effect of pressure drops or dust devils occurring at low altitude next to the lander. Here, we analyze the effect of acoustic emission whose sources are not local but at high altitude or distant from the lander. Indeed, infrasonic waves have been suggested as potential candidates to explain some of the events observed by the SEIS instrument (Martire et al., 2020). Can they explain the polarized background noise of SEIS?

On Earth, winds are known to generate infrasound (Cuxart et al., 2016; Posmentier, 1974). Posmentier (1974) reported, for example, infrasound at 1 Hz of about $1,500 \text{ nbar}^2/\text{Hz}$ in power ($15 \text{ mPa}^2/\text{Hz}$) for wind speeds of 40 m/s at 10 km of altitude. Let us use these Earth observations for a rough estimation of the possible strength of acoustic pressure at the surface of Mars, considering a source correction term and the propagation from the source altitude to the ground of Mars.

For the source, following Goldreich and Keeley (1977), the emitted acoustic pressure at the source in the atmosphere is $\rho v_H^2 \left(\frac{\lambda}{H}\right)^{2/3}$, where ρ , v_H , λ , and H are the atmosphere density, horizontal wind velocity, large eddies' correlation length and size, taken as comparable to the atmosphere height scale by Goldreich and Keeley (1977). The propagation term from the source down to the ground is $\frac{\sqrt{e^{d/H}}}{d}$, where d is the altitude of the source. We can then predict from Earth observations the expected acoustic pressure on the ground on Mars.

On Mars, possible sources are the turbulent wind regimes occurring during most of the daytime within the flow predicted by general circulation models (GCM) for sols 210 and 310, with typical velocities of 20 m/s at about 1 km of altitude. The simple extrapolation presented above, for similar correlation length of eddies, gives an acoustic pressure amplitude at the ground of $\Delta P = 0.2 \text{ mPa}/\text{Hz}^{1/2}$. This value is smaller by about 20, as compared to the Earth case.

Acoustic emission in the atmosphere has a wind-squared dependency, although the wind is not the local one but the wind generating the acoustic emission. The frequency dependency of this acoustic source can be estimated with a Kolmogorov inertial-subrange model (e.g., Shields, 2005) and therefore with a frequency dependency of $f^{-7/3}$.

When such acoustic signals reach the ground at the SEIS location, they generate a reflected acoustic wave and a transmitted P and S wave in the solid planet. Can it explain part of the observed signals? We neglect here the effect of surface topography on acoustic emission (Howe, 1991) because, the landing site is flat and also because as demonstrated below, the acoustic waves of interest have incident angles between 15° and 30° and are mostly related to high altitude winds.

In order to estimate the amplitude and, if any, polarization properties of such acoustic emission when hitting the ground, we consider again the half space brecciated bedrock model used in the previous section. We consider a simple, isotherm atmosphere at 220 K and 700 Pa, for which the sound speed is about 250 m/s. Reflection and transmission coefficients are computed following Aki and Richards (2002) in the case of a fluid/solid interface. Note that analytical expressions are given by Gualtieri et al. (2014) and Zhang et al. (2018), as well as discussion of the critical angles for the ocean-bottom case. These analytical expressions can be used in our case of crust-atmosphere interface as the atmosphere is a fluid.

The pressure to seismic wave ground velocity conversion coefficients, shown in Figure 18, are about $5 \times 10^{-7} \text{ m/s/Pa}$ on the vertical component and comparable on the horizontal component between the two extreme critical angles, of about 15° and 30° , respectively. With a surface acoustic pressure of $0.2 \text{ mPa}/\text{Hz}^{1/2}$, this provides an estimated ground velocity amplitude of about $10^{-10} \text{ m/s}/\text{Hz}^{1/2}$.

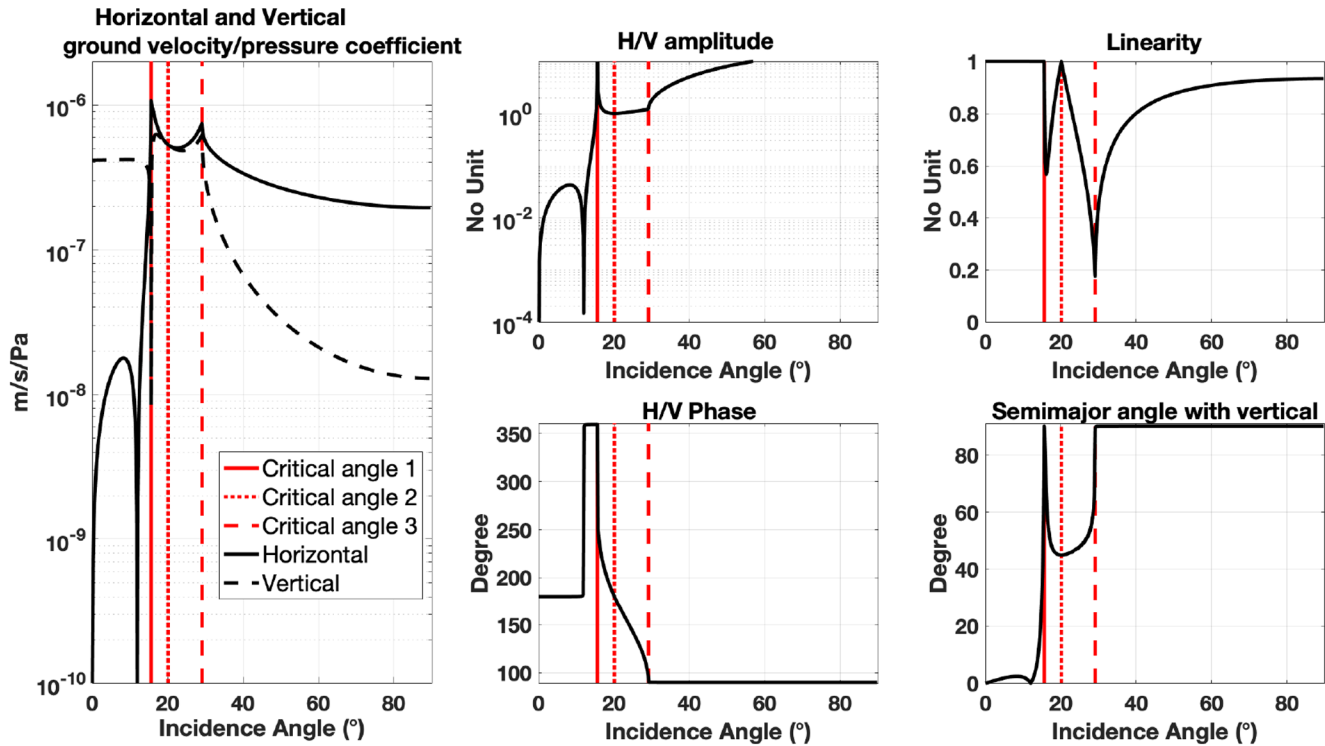


Figure 18. Transmission coefficient between the pressure amplitude of an acoustic wave and the horizontal and vertical ground velocity and impacts in terms of ground ellipticity. The left figure provides the transmission coefficient, as a function of incidence of the pressure wave with respect to vertical, between the amplitude of the pressure wave and the vertical and horizontal ground velocities for a simple interface between Mars' atmosphere (with sound speed of 250 m/s and atmospheric density of 0.017 kg/m³) and a brecciated bedrock (V_p and V_s of 926 and 512 m/s, respectively and density of 2,600 kg/m³). The two critical angles and the one canceling the P transmitted wave are detailed in the text and are shown by the three red lines (first critical angle related to P, angle for no P transmission, and second critical angle related to S). The two middle figures show the amplitude and phase of the H/V ratio, as a function of incidence angle. Below the first critical angle of 15.6 degrees, the transfer coefficients are all real. They start to be complex after the first critical angle, with a variation from 360° to 90° of the H/V phase, until the second critical angle is reached, for an inclination of 29.1°. Then the H/V phase remains 90°. The last panel shows the linearity and the inclination of the semi-major axis of the elliptical signal. For linearity of 1, the semi-major axis is the axis of linear polarization. When the incidence angle increases from the first critical angle to the incidence canceling transmitted P, the linearity decreases down to about 0.6 before reaching 1 again for an incidence angle of 20.1°. The angle of the semi-major axis varies from 90° to 45° with respect to vertical. The same type of variation occurs between the 20.1° incidence and the second critical angle, with the linearity decreasing down to about 0.2 for the third critical angle and again a rotation of the semi-major axis. The semi-major axis remains vertically oriented after the second critical angle, while the linearity is growing toward 1 for large incidences.

Figure 18 shows that a specific feature of these incident acoustic waves is to generate, for incidence angles in the range between the two critical angles, horizontal ground displacement amplitude larger than the vertical one, as well as an elliptical polarization with a semi-major axis inclined with respect to vertical, because the H/V phase delay is different from $\pi / 2$.

Figure 18 also shows that the variation of the linearity with the incidence angle starts from 1 at the first critical angle ($\sin i_{c1} = \frac{c_{\text{atm}}}{v_p}$), decreased to about 0.6 before reaching 1 again for the second critical angle ($\sin i_{c2} = \frac{c_{\text{atm}}}{v_s}$). It then decreases again down to 0.2 before growing again toward an almost horizontal linear polarization state. For the first critical incident angles i_{c1} , the angle between the semi-major vector and the vertical is 90°. For increasing incident angles, the semi-major angle with the vertical is decreasing down to 45°, which is reached for the second critical incident angle i_{c2} .

The angle of 45 degrees is consistent with the measured semi-major incident angle for frequency above 0.3 Hz. This angle is measured most of the time except during the very low wind period between 18:00 LMST and 22:00 LMST (Figure 7). An acoustic pressure source is therefore the only mechanism able to generate, for 1-D models, ellipticity with an oblique semi-major axis with respect to vertical. However, the

pressure frequency dependency, for a Kolmogorov inertial-subrange model, is proportional to $f^{-7/6}$. The pressure, P , is related to the ground velocity, V , through $P = \rho cV$ where ρ and c are the atmosphere density and sound speed, leading to a ground acceleration amplitude proportional to $f^{-1/6}$. This frequency dependence is different from the seismic observation, where the spectrum amplitude is proportional to $1/f$ at LF and to f at HF (Figure 3). Note that during the night, wind might remain relatively large at a few kilometers altitude above the surface (the so-called low-level jet, see Banfield et al., 2020) and this may provide a background noise.

5.6. Propagating Polarized Seismic Waves

Finally, let us consider seismic waves as a potential source of noise. During windy conditions—that is, from midnight to about 18:00 LMST, we have already seen that above 0.3 Hz, the polarization is elliptical and tilted in the vertical plane and below 0.3 Hz, the polarization is elliptical clock-wise and anticlockwise in the horizontal plane. For comparison, Figure A3 shows the polarization attributes on Earth for station SSB and TAM of the GEOSCOPE Network. Rayleigh wave elliptical polarization in the vertical plane can be clearly identified between 0.1 and 1 Hz, that is in the secondary microseism frequency band (e.g., Schimmel, Stutzmann, Ardhuin, & Gallart, 2011; Stutzmann et al., 2009; Tanimoto & Rivera, 2005). Between 0.05 and 0.1 Hz, there is more equipartition between Rayleigh and Love waves (Nishida, 2014; Nishida et al., 2008). Horizontal polarization related to tilt is observed below 0.04 Hz (e.g., Koper & Hawley, 2010).

The analysis of the measured seismic polarization on Mars suggest that a large part of the signals have wind-induced origins. It is therefore better to concentrate on the “quiet zone” time window between 18:00 and 22:00, when the local wind is extremely small and the corresponding local or regional noise sources discussed above weaken.

Whereas during most of the time, the HF signals are polarized in the vertical plane, between 18:00 and 22:00 they are polarized in the horizontal plane (Figure 7) and the linearity becomes closer to 0.9. It therefore suggests a background of linearly polarized signals, relatively isotropic in azimuth. These signals may correspond to seismic propagating waves.

We speculate that this low-level background noise above 0.3 Hz and between 18 and 22 LMST hours is the only candidate for a seismic wave background noise. The corresponding azimuths are relatively isotropic. All events detected so far have shown large evidence of scattering, including below 1 Hz (Giardini et al., 2020; Lognonne et al., 2020). The polarization of these events has been analyzed (Clinton et al., 2020) and only for few of them, a polarization associated to P or S could be measured. None of these events showed an elliptical polarization in the vertical plane as expected for Rayleigh waves. In its multidiffusion regime, seismic background noise will therefore have about 10 times more energy in S waves than P waves (Aki, 1992; Papanicolaou et al., 1996) which support mostly horizontally linearly polarized seismic waves. Multiple conversions of these waves would also generate surface waves, dominantly Love waves if S-wave horizontally polarized are dominant.

Background seismic noise may be generated by conversion of acoustic waves or by thermal cracks. In the evening, when the ground is cooling, HF seismic signals associated with surface thermal cracks are detected (Dahmen et al., 2020). One possibility, that needs to be confirmed, is that the observed horizontally polarized signals are the LF component of these thermal cracks.

6. Conclusion

Seismic noise on Mars, recorded by the InSight station during the first 491 sols of the mission, is 500 times smaller than on Earth at night around 0.2 Hz and the lowest noise level reaches -200 dB in acceleration. The noise level in the frequency band 0.03–1 Hz is higher during the day at all frequencies and, furthermore, the vertical axis is noisier during daytime than the horizontal.

The time-frequency polarization of seismic noise on Mars is investigated using the method developed for studying Earth noise (Schimmel, Stutzmann, Ardhuin, & Gallart, 2011; Stutzmann et al., 2009). The key point is the use of the DOP which enables us to extract signals with stable polarization as a function of

time and frequency, whatever their amplitude. Whereas on Earth, we can clearly identify Rayleigh waves polarization in the secondary microseismic frequency band and both Rayleigh and Love waves in the primary microseismic frequency band, on Mars the polarization is more complex.

We measured polarized signals at all frequencies between 0.03 and 1 Hz and at all times. Linearly polarized glitches can be clearly identified and they are more abundant during the night as also observed by Scholtz et al. (2020). Signals with elliptical polarization have different patterns at low (0.03–0.3 Hz) and high (0.3–1 Hz) frequencies. At LF, these signals are always polarized in the horizontal plane with both clockwise and anticlockwise motion. At HF, they are polarized in the vertical plane and the major axis is tilted with respect to the vertical, except between 18:00 and 22:00 LMST time. The measured azimuths are different in the two frequency bands but they both strongly vary over LMST time with abrupt changes around sunset and sunrise. They also display progressive variations from one sol to another following seasonal changes, along the 491 sols of the mission. These azimuths are correlated with wind direction in both frequency ranges, particularly during the day.

We investigated the possible origins of this elliptically polarized noise. Results for the different noise source candidates are summarized in Table 1. We excluded sensor self-noise and lander noise as they only generate linearly polarized signals. LSA or tether noise may only explain a small fraction of the polarized signals, which have linearity above 0.8. Compliance effect generated by pressure waves propagating along the planet surface at the wind speed is a good candidate for explaining part of the HF polarized signals. The resulting elliptical polarization is in the vertical plane as our observation above 0.3 Hz, but this mechanism cannot explain the measured inclined semi-major axis of the polarization ellipse. The only mechanism that we have found which can generate a tilt of the vertical ellipse, corresponds to acoustic waves coming from the atmosphere and hitting the ground at the SEIS location with an incident angle around 15°–30°.

Finally, it is only during low wind time, that is between 18:00 and 24:00 LMST at frequency higher than 0.3 Hz, that we can investigate the seismic background noise. The signals are polarized in the horizontal plane, they are more linear and they have isotropic azimuths which is not the case for the rest of the sol. We consider that this low-level background signal is the only candidate for the seismic wave background noise. In the shallow layers corresponding to a multiple-diffusion medium, this seismic background noise would mostly correspond to S-waves and Love waves, which is consistent with almost linear polarization in the horizontal plane. Sources of these seismic waves are still to be discovered.

Table 1
Summary of the Noise Observations and Their Possible Sources

	Vertical power ($10^{-20} \text{ m}^2/\text{s}^4/\text{Hz}$)	LF polarization (0.03–0.3 Hz)	HF polarization (0.3–1 Hz)	Azimuth
Observations	$e^2 + 0.0058 \frac{\langle v^2 \rangle}{f^2} + 0.44 f^2 < v^2 >$	Ellipse in the horizontal plane	Inclined ellipse in the vertical plane	Varying over LMST and season
Sensor self-noise	$e^2 = 0.125 f^{-1.2} + 0.49 + 2 f^{\beta}$	None	None	None
Lander noise	$0.1 \langle v^2 \rangle^2 f^{2/3}$	Linear ($L = 1$)	Linear ($L = 1$)	Lander related
LSA/Tether noise	Expected < 100 by design	$0.8 < L < 1$	$0.8 < L < 1$	Tether or feet related
Pressure waves noise	$> \frac{f^{-0.4}}{22.5} \times (\text{observation} - e^2)$	Ellipse in the vertical plane	Ellipse in the vertical plane	Toward the source
Acoustic emission noise	$0.015 \langle v^2 \rangle^2 f^{-1/6}$	Inclined ellipse in the vertical plane	Inclined ellipse in the vertical plane	Toward the source
Micro-seismic noise	Less than acoustic emission noise	Linear or elliptical	Linear or elliptical	Toward the source or random in scattered medium

Note. Observations are from Lognonne et al. (2020), Giardini et al. (2020), and this study. Sensor self-noise is from Lognonne et al. (2019), with an approximation valid between 0.02 and 1 Hz. Lander noise is from Murdoch et al. (2017). A lower bound of the pressure noise is estimated from the ratio between day VBBZ noise and the coherent part of it with respect to the product of wind by pressure, the later recorded by APSS (see Supplement 1 of Lognonne et al. [2020]). This ratio varies from three at 0.1 to 4.6 at 1 Hz. L is the polarization linearity. Acoustic emission noise estimation is from Earth scaling as developed in the text. Other wind related noise sources on the horizontal axis could be considered, such as wind-induced ground cooling. All frequencies are in Hz.

Appendix: Polarization Decomposition

Let us consider the frame $(Ox'y'z')$ corresponding respectively to the semi-major axis, semi-minor axis, and to the direction perpendicular to the elliptical particle motions. In this axis, the particle motion can be expressed as:

$$\begin{aligned}x' &= A \cos(\omega t), \\y' &= A(1-L)\sin(\omega t), \\z' &= 0,\end{aligned}\quad (4)$$

where ω , A , and L are the angular frequency, the intensity of the particle motion, and the polarization linearity, respectively.

Figure 4 shows a sketch of the ellipse of polarization and the Euler angles. Let us search first the three Euler angles necessary to rotate this frame into the one given by the polarization analysis, which characterizes the elliptical particle motion with three angles: (1) the incidence angle, I_p , of the semi-major axis x' with the vertical axis, (2) the azimuth, ψ_p , between North and the projection of the semi-major axis on the horizontal plane, and (3) the angle θ_p between z' , that is the perpendicular to the plane $x'-y'$ and its projection on the horizontal plane. The nutation angle θ is equal to $\pi/2 - \theta_p$. The two other angles can be obtained by taking the first column of the Euler rotation matrix, which provides the components of the unit vector x' in the reference N, W, Z^+ basis (noted xyz hereafter) after the Euler rotation. This can be written as

$$\mathbf{e}_{x'} = (\cos \psi \cos \phi - \sin \psi \sin \phi \cos \theta) \mathbf{e}_x + (\sin \psi \cos \phi + \cos \psi \sin \phi \cos \theta) \mathbf{e}_y + \sin \theta \sin \phi \mathbf{e}_z. \quad (5)$$

The scalar product of this vector with the vertical axis is by definition the cosine of the incidence angle, so we have

$$\cos(I_p) = \sin(\theta) \sin(\phi). \quad (6)$$

We then get the azimuth by computing the scalar product of the horizontal projection of $\mathbf{e}_{x'}$ (with normalization to 1) on North, which gives

$$\cos(\psi_p) = \frac{\cos \psi \cos \phi - \sin \psi \cos \theta \sin \phi}{\sqrt{\cos^2 \phi + \cos^2 \theta \sin^2 \phi}}, \quad (7)$$

We also have:

$$\cos(\psi_p) = \cos(\psi + \delta\psi) = \cos(\psi) \cos(\delta\psi) - \sin(\psi) \sin(\delta\psi) \quad (8)$$

By analogy between Equations 6 and 7, we get:

$$\cos(\delta\psi) = \frac{\cos(\phi)}{\sqrt{\cos^2 \phi + \cos^2 \theta \sin^2 \phi}} \quad (9)$$

and

$$\sin(\delta\psi) = \frac{\cos(\theta) \sin(\phi)}{\sqrt{\cos^2 \phi + \cos^2 \theta \sin^2 \phi}} \quad (10)$$

and finally $\tan \delta\psi = \cos \theta \tan \phi$ and we get the last and third Euler angle. Let us now assume that the particle motion is expressed as a vertical/horizontal elliptical motion and a linearly polarized one, the later having

a phase delay ϕ_N with respect to the vertical amplitude of the elliptical motion. In the (xyz) frame, we can express the particle motion after Euler rotation on the three components as:

$$x = E_{xx}A \cos(\omega t) + E_{xy}A(1-L)\sin(\omega t), \quad (11)$$

$$y = E_{yx}A \cos(\omega t) + E_{yy}A(1-L)\sin(\omega t), \quad (12)$$

$$z = E_{zx}A \cos(\omega t) + E_{zy}A(1-L)\sin(\omega t), \quad (13)$$

where E_{ij} are the elements of the Euler rotation matrix. This particle motion can also be written as the composition of the two (linear and elliptical) motions:

$$x = H_x \sin(\omega t) + N \cos \psi_N \cos(\omega t - \phi_N), \quad (14)$$

$$y = H_y \sin(\omega t) + N \sin \psi_N \cos(\omega t - \phi_N), \quad (15)$$

$$z = Z \cos(\omega t) + N_z \cos(\omega t - \phi_N), \quad (16)$$

where $H_x, H_y, Z, N, \psi_N, N_z$ are the x, y components of the elliptical motion, the z' component of the elliptical motion, the horizontal linear motion, the azimuth of the horizontal motion, and the vertical linear motion, respectively. After replacing, these six components can be determined by equating the six cosine and sin equations as functions of: A , of the four parameters of the particle motion in the $Oxyz$ (L, ψ_P, θ_P, I_P) and of the phase delay parameter ϕ_N between the elliptical and linear motions. We then get:

$$\begin{aligned} \tan(\psi_N) &= \frac{E_{yx}}{E_{xx}}, \\ \frac{N}{A} &= \frac{\sqrt{E_{xx}^2 + E_{yx}^2}}{\cos(\phi_N)}, \\ \frac{H_x}{A} &= E_{xy}(1-L) - \frac{N}{A} \cos(\psi_N) \sin(\phi_N), \\ \frac{H_y}{A} &= E_{yy}(1-L) - \frac{N}{A} \sin(\psi_N) \sin(\phi_N), \\ \frac{N_z}{A} &= \frac{E_{zy}(1-L)}{\sin(\phi_N)}, \\ \frac{Z}{A} &= E_{zx} - \frac{E_{zy}(1-L)}{\tan(\phi_N)}. \end{aligned}$$

We note that the smaller the phase shift ϕ_N is, the larger will be the vertical components of the linear motion, as it is the only one matching the sin component on the vertical component. The azimuth with respect to North in the N, E of the horizontal components of the elliptical polarized motion is $\tan(\psi_H) = -\frac{H_y}{H_x}$ while the one of the linear component will be $-\phi_N$. All components for Z downward are the opposite for N_z and Z .

Data Availability Statement

Data corresponding to this article are in Stutzmann et al. (2020). Seis raw data are in “InSight Mars SEIS Data Service together with IPGP, JPL, CNES, ETHZ, ICL, MPS, ISAE-Supaero, LPG, MFSC” (2019) with doi:https://doi.org/10.18715/SEIS.INSIGHT.XB_2016.

Acknowledgments

This is the InSight contribution number 143 and IPGP contribution number 4183. We acknowledge NASA, CNES, their partner agencies and institutions (UKSA, SSO, DLR, JPL, IPGP-CNRS, ETHZ, IC, MPS-MPG) and the flight operations team at JPL, SISMOC, MSDS, IRIS-DMC, and PDS for providing SEED SEIS data. French authors are supported by ANR MAGIS (ANR-19-CE31-0008-08) and by CNES for SEIS science support. A. Horleston is supported by the UK Space Agency through grant #ST/R002096/1. M. Schimmel is supported by the SANIMS project (RTI2018-095594-B-I00, MICINN, Spain).

References

Aki, K. (1992). Scattering conversions P to S versus S to P. *Bulletin of the Seismological Society of America*, 82(4), 1969–1972.

Aki, K., & Richards, P. G. (2002). Chapter 5 - Plane waves in homogeneous media and their reflection and transmission at a plane boundary. In J. Ellis (Ed.), *Quantitative seismology* (pp. 123-192). University Science Books.

Anderson, D. L., Miller, W., Latham, G., Nakamura, Y., Toksöz, M., Dainty, A., et al. (1977). Seismology on mars. *Journal of Geophysical Research*, 82(28), 4524–4546.

Ardhuin, F., Gualtieri, L., & Stutzmann, E. (2015). How ocean waves rock the Earth: Two mechanisms explain microseisms with periods 3 to 300 s. *Geophysical Research Letters*, 42(3), 765–772. <https://doi.org/10.1002/2014gl062782>

Banerdt, B., Smrekar, S., Banfield, D., Giardini, D., Golombek, M., Johnson, C., et al. (2020). Initial results from the InSight mission on Mars. *Nature Geoscience*, 13, 183–189. <https://doi.org/10.1038/s41561-020-0544-y>

Banfield, D., Spiga, A., Newman, C., Forget, F., Lemmon, M., Lorenz, R., et al. (2020). The atmosphere of Mars as observed by InSight. *Nature Geoscience*, 13, 190. <https://doi.org/10.1038/s41561-020-0534-0>

Berbellini, A., Schimmel, M., Ferreira, A. M., & Morelli, A. (2019). Constraining S-wave velocity using Rayleigh wave ellipticity from polarization analysis of seismic noise. *Geophysical Journal International*, 216(3), 1817–1830. <https://doi.org/10.1093/gji/ggy512>

Beyreuther, M., Barsch, R., Krischer, L., Megies, T., Behr, Y., & Wassermann, J. (2010). ObsPy: A Python toolbox for seismology. *Seismological Research Letters*, 81(3), 530–533.

Ceylan, S., Clinton, J., Giardini, D., Bose, M., Charalambous, C., van Driel, M., et al. (2020). Companion guide to the Marsquake catalog from InSight, sols 0-478: Data content and non-seismic events. *Physics of the Earth and Planetary Interiors*, 309. <https://doi.org/10.1016/j.pepi.2020.106597>

Charalambous, C., Stott, A., Pike, W., McClean, W., Warren, T., Spiga, A., et al. (2020). A comodulation analysis of atmospheric energy injection into the ground motion at InSight, Mars. *Earth and Space Science Open Archive*. <https://doi.org/10.1002/essoar.10503206.1>

Clinton, J. F., Ceylan, S., van Driel, M., Giardini, D., Stähler, S. C., Böse, M., et al. (2020). The Marsquake catalogue from InSight, sols 0-478. *Physics of the Earth and Planetary Interiors*, 1–99. <https://doi.org/10.31219/osf.io/ws967>

Crawford, W. C., Webb, S. C., & Hildebrand, J. A. (1991). Seafloor compliance observed by long-period pressure and displacement measurements. *Journal of Geophysical Research*, 96(B10), 16151–16160.

Cuxart, J., Tatray, D., Weidinger, T., Kircsi, A., Jozsa, J., & Kiss, M. (2016). Infrasound as a detector of local and remote turbulence. *Boundary-Layer Meteorology*, 159(2), 185–192.

Dahmen, N. L., Clinton, J. F., Ceylan, S., van Driel, M., Giardini, D., Khan, A., et al. (2020). Super high frequency events: A new class of events recorded by the InSight seismometers on Mars. *Journal of Geophysical Research: Planets*, e2020JE006599. <https://doi.org/10.1029/2020JE006599>

Farrell, W. (1972). Deformation of the Earth by surface loads. *Reviews of Geophysics*, 10(3), 761–797.

Fayon, L., Knapmeyer-Endrun, B., Lognonné, P., Bierwirth, M., Kramer, A., & Delage, P. (2018). A numerical model of the SEIS leveling system transfer matrix and resonances: Application to SEIS rotational seismology and dynamic ground interaction. *Space Science Reviews*, 214(8), 119. <https://doi.org/10.1007/s11214-018-0555-9>

Garcia, R. P., Kenda, B., Kawamura, T., Spiga, A., Murdoch, N., Lognonné, P., et al. (2020). Pressure effects on the SEIS-InSight instrument, improvement of the seismic records and characterization of the long period atmospheric waves from ground displacement. *Journal of Geophysical Research: Planets*, 125, e2019JE006278. <https://doi.org/10.1029/2019JE006278>

Giardini, D., Lognonne, P., Banerdt, W., Pike, W., Christensen, U., Ceylan, S., et al. (2020). The seismicity on Mars. *Nature Geoscience*, 13, 205–212. <https://doi.org/10.1038/s41561-020-0539-8>

Goldreich, P., & Keeley, D. (1977). Solar seismology. II-The stochastic excitation of the solar p-modes by turbulent convection. *The Astrophysical Journal*, 212, 243–251.

Golombek, M., Warner, N., Grant, J., Hauber, E., Ansen, V., Weitz, C., et al. (2020). Geology of the InSight landing site, Mars. *Nature Geoscience*, 11, 1–11. <https://doi.org/10.1038/s41467-020-14679-1>

Gualtieri, L., Stutzmann, E., Farra, V., Capdeville, Y., Schimmel, M., Ardhuin, F., & Morelli, A. (2014). Modelling the ocean site effect on seismic noise body waves. *Geophysical Journal International*, 197(2), 1096–1106. <https://doi.org/10.1093/gji/ggu042>

Hasselmann, K. (1963). A statistical analysis of the generation of microseisms. *Reviews of Geophysics*, 1, 177–209.

Haubrich, R. A., & McCamy, K. (1969). Microseisms: Coastal and pelagic sources. *Reviews of Geophysics*, 7(3), 539–571.

Howe, M. (1991). Surface pressures and sound produced by turbulent flow over smooth and rough walls. *Journal of the Acoustical Society of America*, 90, 1041–1047. <https://doi.org/10.1121/1.402292>

InSight Mars SEIS Data Service together with IPGP, JPL, CNES, ETHZ, ICL, MPS, ISAE-Supaero, LPG, MFSC. (2019). <https://doi.org/10.18715/SEIS.INSIGHT.XB2016>

Kenda, B., Drilleau, M., Garcia, R., Kawamura, T., Murdoch, N., Compaire, N., et al. (2020). Subsurface structure at the InSight landing site from compliance measurements by seismic and meteorological experiments. *Journal of Geophysical Research*, 125, e2020JE006387. <https://doi.org/10.1029/2020JE006387>

Kenda, B., Lognonné, P., Spiga, A., Kawamura, T., Kedar, S., Banerdt, W. B., et al. (2017). Modeling of ground deformation and shallow surface waves generated by Martian dust devils and perspectives for near-surface structure inversion. *Space Science Reviews*, 211(1–4), 501–524. <https://doi.org/10.1007/s11214-017-0378-0>

Koper, K. D., & Hawley, V. L. (2010). Frequency dependent polarization analysis of ambient seismic noise recorded at a broadband seismometer in the central United States. *Earthquake Science*, 23(5), 439–447.

Lognonne, P., Banerdt, W. B., Giardini, D., Pike, W. T., Christensen, U., Laudet, P., et al. (2019). SEIS: InSight's seismic experiment for internal structure of Mars. *Space Science Reviews*, 215(1), 1–170. <https://doi.org/10.1007/s11214-018-0574-6>

Lognonne, P., Banerdt, W., Pike, W. T., Giardini, D., Christensen, U., et al. (2020). Constraints on the shallow elastic and anelastic structure of Mars from InSight seismic data. *Nature Geoscience*, 13, 213–220. <https://doi.org/10.1038/s41561-020-0536-y>

Lognonné, P., & Mosser, B. (1993). Planetary seismology. *Surveys in Geophysics*, 14(3), 239–302. <https://doi.org/10.1007/BF00690946>

Lorenz, R., Kedar, S., Murdoch, N., Lognonné, P., Kawamura, T., Mimoun, D., & Banerdt, B. (2015). Seismometer Detection of Dust Devil Vortices by Ground Tilt. *Bulletin of the Seismological Society of America*, 105(6), 3015–3023. <https://doi.org/10.1785/0120150133>

Martire, L., Garcia, R. F., Rolland, L., Spiga, A., Lognonné, P., Banfield, D., et al. (2020). Martian infrasound: Numerical modeling and analysis of InSight's data. *Journal of Geophysical Research: Planets*, 125, e2020JE006376. <https://doi.org/10.1029/2020JE006376>

McNamara, D. E., & Buland, R. P. (2004). Ambient noise levels in the continental United States. *Bulletin of the Seismological Society of America*, 94(4), 1517–1527.

- Mimoun, D., Murdoch, N., Lognonné, P., Hurst, K., Pike, T., Hurley, J., et al. (2017). The noise model of the SEIS seismometer of the InSight mission to Mars. *Space Science Reviews*, 211(1–4), 383–428. <https://doi.org/10.1007/s11214-017-0409-x>
- Murdoch, N., Alazard, D., Knapmeyer-Endrun, B., Teanby, N. A., & Myhill, R. (2018). Flexible mode modelling of the InSight lander and consequences for the SEIS instrument. *Space Science Reviews*, 214(117), 1–24. <https://doi.org/10.1007/s11214-018-0553-y>
- Murdoch, N., Kenda, B., Kawamura, T., Spiga, A., Lognonné, P., Mimoun, D., & Banerdt, B. (2017). Estimations of the seismic pressure noise on Mars determined from Large Eddy Simulations and demonstration of pressure decorrelation techniques for the InSight mission. *Space Science Reviews*, 211(1–4), 457–483.
- Nishida, K. (2014). Source spectra of seismic hum. *Geophysical Journal International*, 199(1), 416–429.
- Nishida, K., Kawakatsu, H., Fukao, Y., & Obara, K. (2008). Background Love and Rayleigh waves simultaneously generated at the Pacific Ocean floors. *Geophysical Research Letters*, 35(16), L16307. <https://doi.org/10.1029/2008GL034753>
- Nishikawa, Y., Lognonné, P., Kawamura, T., Spiga, A., Stutzmann, E., Schimmel, M., et al. (2019). Mars' background free oscillations. *Space Science Reviews*, 215(1), 1–26. <https://doi.org/10.1007/s11214-019-0579-9>
- Panning, M. P., Pike, W. T., Lognonné, P., Banerdt, W. B., Murdoch, N., Banfield, D., et al. (2020). On-deck seismology: Lessons from InSight for future planetary seismology. *Journal of Geophysical Research: Planets*, 125, e2019JE006353. .
- Papanicolaou, G., Ryzhik, L., & Keller, J. (1996). Stability of the P-to-S energy ratio in the diffusive regime. *Bulletin of the Seismological Society of America*, 86(6), 1107.
- Peterson, J. (1993). Observations and modeling of seismic background noise. *US Geological Survey Technical Report*, 93(322), 1–95.
- Posmentier, E. (1974). 1- to 16-Hz infrasound associated with clear air turbulence predictor. *Journal of Geophysical Research*, 79(12), 1755–1760. <https://doi.org/10.1029/JC079i012p01755>
- Rhie, J., & Romanowicz, B. (2006). A study of the relation between ocean storms and the Earth's hum. *Geochemistry, Geophysics, Geosystems*, 7(10), Q10004. <https://doi.org/10.1029/2006GC001274>
- Romero, P., & Schimmel, M. (2018). Mapping the basement of the Ebro Basin in Spain with seismic ambient noise autocorrelations. *Journal of Geophysical Research: Solid Earth*, 123(6), 5052–5067. <https://doi.org/10.1029/2018jb015498>
- Roult, G., & Crawford, W. (2000). Analysis of 'background' free oscillations and how to improve resolution by subtracting the atmospheric pressure signal. *Physics of the Earth and Planetary Interiors*, 121(3–4), 325–338.
- Samson, J., & Olson, J. (1980). Some comments on the descriptions of the polarization states of waves. *Geophysical Journal of the Royal Astronomical Society*, 61, 115–129.
- Savoie, D., Richard, A., Goutaudier, M., Lognonné, P. H., Hurst, K., Maki, J. N., et al. (2020). Finding SEIS North on Mars: Comparisons between SEIS sundial, Inertial and Imaging measurements and consequences for seismic analysis. *Earth and Space Science*. <https://doi.org/10.1002/essoar.10503306.1>
- Schimmel, M., & Gallart, J. (2003). The use of instantaneous polarization attributes for seismic signal detection and image enhancement. *Geophysical Journal International*, 155(2), 653–668.
- Schimmel, M., & Gallart, J. (2004). Degree of polarization filter for frequency-dependent signal enhancement through noise suppression. *Bulletin of the Seismological Society of America*, 94(3), 1016–1035.
- Schimmel, M., Stutzmann, E., Arduin, F., & Gallart, J. (2011). Polarized Earth's ambient microseismic noise. *Geochemistry, Geophysics, Geosystems*, 12, Q07014. <https://doi.org/10.1029/2011GC003661>
- Schimmel, M., Stutzmann, E., & Gallart, J. (2011). Using instantaneous phase coherence for signal extraction from ambient noise data at a local to a global scale. *Geophysical Journal International*, 184(1), 494–506. <https://doi.org/10.1111/j.1365-246x.2010.04861.x>
- Scholtz, J.-R., Widmer-Schmidrig, R., Davis, P., Lognonné, P., Pinot, B., Garcia, R., et al. (2020). Detection, analysis and removal of glitches from InSight's seismic data from Mars. *Journal of Geophysical Research*, 7, e2020EA001317. <https://doi.org/10.1029/2020EA001317>
- Shields, F. (2005). Low-frequency wind noise correlation in microphone arrays. *Journal of the Acoustical Society of America*, 117(6), 3489–3496.
- Sorrells, G. G. (1971). A preliminary investigation into the relationship between long-period seismic noise and local fluctuations in the atmospheric pressure field. *Geophysical Journal International*, 26(1–4), 71–82.
- Spiga, A., Banfield, D., Teanby, N. A., Forget, F., Lucas, A., Kenda, B., et al. (2018). Atmospheric science with InSight. *Space Science Reviews*, 214(7), 1–64. <https://doi.org/10.1007/s11214-018-0543-0>
- Stockwell, R. G., Mansinha, L., & Lowe, R. P. (1996). Localization of the complex spectrum: The S transform. *IEEE Transactions on Signal Processing*, 44(4), 998–1001.
- Stutzmann, E., Arduin, F., Schimmel, M., Mangeney, A., & Patau, G. (2012). Modelling long-term seismic noise in various environments. *Geophysical Journal International*, 191(2), 707–722. <https://doi.org/10.1111/j.1365-246x.2012.05638.x>
- Stutzmann, E., Schimmel, M., Lognonné, P. (2020). Data from the article: The polarization of ambient noise on Mars. <https://doi.org/10.18715/IPGP.2020>
- Stutzmann, E., Schimmel, M., Patau, G., & Maggi, A. (2009). Global climate imprint on seismic noise. *Geochemistry, Geophysics, Geosystems*, 10(11), Q11004. <https://doi.org/10.1029/2009gc002619>
- Suemoto, Y., Ikeda T., & Tsuji, T. (2020). Temporal variation and frequency dependence of seismic ambient noise on Mars from polarization analysis. *Geophysical Research Letters*, 47(13), e2020GL087123. <https://doi.org/10.1029/2020GL087123>
- Tanimoto, T. (2007). Excitation of normal modes by non-linear interaction of ocean waves. *Geophysical Journal International*, 168(2), 571–582.
- Tanimoto, T., Ishimaru, S., & Alvizuri, C. (2006). Seasonality in particle motion of microseisms. *Geophysical Journal International*, 166(1), 253–266. <https://doi.org/10.1111/j.1365-246x.2006.02931.x>
- Tanimoto, T., & Rivera, L. (2005). Prograde Rayleigh wave particle motion. *Geophysical Journal International*, 162(2), 399–405.
- Tanimoto, T., Um, J., Nishida, K., & Kobayashi N. (1998). Earth's continuous oscillations observed on seismically quiet days. *Geophysical Research Letter*, 25(10), 1553–1556.
- Van Hoolst, T., Dehant, V., Roosbeek, F., & Lognonné, P. (2003). Tidally induced surface displacements, external potential variations, and gravity variations on Mars. *Icarus*, 161(2), 281–296. [https://doi.org/10.1016/S0019-1035\(02\)00045-3](https://doi.org/10.1016/S0019-1035(02)00045-3)
- Zhang, G., Hao, C., & Yao, C. (2018). Analytical study of the reflection and transmission coefficient of the submarine interface. *Acta Geophysica*, 66, 449–460. <https://doi.org/10.1007/s11600-018-0153-y>
- Zürn, W., & Wielandt, E. (2007). On the minimum of vertical seismic noise near 3 mHz. *Geophysical Journal International*, 168(2), 647–658. <https://doi.org/10.1111/j.1365-246x.2006.03189.x>